IMPACT OF CORDIERITE PARTIAL FLOW PARTICULATE FILTER ON A LIGHT-DUTY DIESEL VEHICLE THERMAL EFFICIENCY AND PARTICLE EMISSION

DANG QUANG HUY

A THESIS SUBMITTED IN PARTIAL FULFILLMENT

OF THE REQUIREMENT FOR THE DEGREE OF

MASTER OF ENGINEERING IN AUTOMOTIVE AND ADVANCED TRANSPORTATION ENGINEERING

SCHOOL OF ENGINEERING

KING MONGKUT'S INSTITUTE OF TECHNOLOGY LADKRABANG

2024

KMITL-2024-EN-M-277-219

Thesis	Impact of Cordierite Partial Flow Particulate Filter on a Light-Duty Diesel Vehicle Thermal Efficiency and Particle Emission
Student	Mr. Dang Quang Huy
Student ID.	65016115
Degree	Master of Engineering
Program	Automotive and Advanced Transportation Engineering (International Program)
Year	2024
Thesis Advisor	Asst. Prof. Dr. Mek Srilomsak
Co-Thesis Advisor	Dr. Sompong Srimanosaowapak
Co-Thesis Advisor	Prof. Dr. Hidenori Kosaka

ABSTRACT

The stringent emission regulations raise significant concerns regarding harmful gases and particles emitted from diesel vehicle exhaust, adversely affecting human health and the environment. This study investigates the impact of a cordierite partial-flow diesel particulate filter (P-DPF) on a light-duty diesel vehicle's thermal efficiency and emission characteristics. The evaluation utilizes commercial fuel B10 and biodiesel B100 to assess the feasibility of P-DPF for an aged untreated diesel vehicle. The filter's microstructure is inspected using scanning electron microscopy to better understand the characteristics of its substrate. Subsequently, two test setups are conducted on chassis dynamometers: steady-state engine conditions and the new European driving cycle (NEDC) to compare the results with and without P-DPF. The initial test involves testing the vehicle to assess fuel flow rate, brake thermal efficiency, and exhaust emissions at three engine speeds: 1500, 2000, and 2500 rpm, corresponding to four loads: 84, 112, 140, and 160 Nm. The second test evaluates emission factors of regulated pollutants under the NEDC. Analysis shows that the filter's substrate is made of cordierite with a porosity of 66%, while the catalyst material is ceria-zirconia oxide. The pore sizes range mainly from 3-20 μm, with a mean pore size of 14 μm. Installation of P-DPF has a minimal impact on the fuel flow rate due to low backpressure,

increasing by 1.6% and 0.5% with B10 and B100, respectively. Meanwhile, brake thermal efficiency decreases no more than 0.7%. A significant reduction in smoke intensity is observed when P-DPF is installed, with a decrease of over 57% for both fuels. Analysis of NO, CO_2, O_2, and exhaust gas temperature suggests that simultaneous trapping and passive soot oxidation may occur inside the P-DPF through reactions of NO_2 and O_2 with soot at appropriate temperatures. Particulate matter is significantly reduced when P-DPF is installed under NEDC. In particular, particulate number is reduced by 36%, while particulate mass is reduced by 59%. These reductions are attributed to the filtration mechanism of P-DPF that partially traps particulate matter inside the porous walls while allowing the remaining flow through the open channels. Moreover, the catalytic coating within P-DPF reduces CO by up to 20% and total HC by 22%. Installation of P-DPF demonstrates a practical approach to reducing harmful and toxic emissions in older diesel vehicles that lack an after-treatment system with minimal modifications.

Keywords: DPF Microstructure, Thermal Efficiency, Backpressure, Diesel Emissions, Partial Flow Diesel Particulate Filter.

ACKNOWLEDGEMENT

I wish to express my deepest gratitude to the National Science and Technology Development Agency (NSTDA) for awarding me the scholarship through the TAIST-Tokyo Tech program. Additionally, I am profoundly thankful to PAP Prosperity Co. Ltd. and King Mongkut's Institute of Technology Ladkrabang (KMITL) for their generous financial support and for providing a conducive research environment through the Monozukuri program. Without their invaluable support, completing this work would not have been possible.

To my thesis advisor, Assistant Professor Dr. Mek Srilomsak, I am deeply grateful for his enthusiastic support and guidance throughout the entire process. I also wish to acknowledge the invaluable guidance and advice provided by Associate Professor Dr. Preechar Karin. His expertise, experience, and constructive feedback were instrumental in shaping this research. Additionally, I sincerely appreciate my co-advisors, Dr. Sompong Srimanosaowapak from NSTDA and Professor Dr. Hidenori Kosaka from the Tokyo Institute of Technology. Their constructive suggestions and valuable advice significantly enhanced the quality of this work.

I would also like to thank the staff of the School of Engineering, namely Mr. Harit Siriphokakorn and Ms. Benjarat Nuchanart, for their administrative support. Special thanks to Mr. Watanyoo Phairote and senior Mr. Poonnut Thaeviriyakul for their technical assistance. I am also grateful to Ms. Mi Zwe Mon Phyo, Ms. Myat Hsu Thin, and Mr. Plan Teekatasn Cosh for their knowledge transfer and insightful discussions, all of which greatly contributed to this research. Furthermore, I wish to acknowledge the unwavering support from my classmate, Mr. Witchayut Suthanyarat. His assistance in daily life, encouragement, and shared insights have been invaluable to me throughout this journey.

Lastly, I extend my greatest gratitude to my parents, relatives, and colleagues for their unwavering support and encouragement throughout this journey. They have been my rock, providing a solid foundation that enabled me to confidently complete this work.

Dang Quang Huy

12 April 2024

TABLE OF CONTENTS

Page

LIST OF TABLES

LIST OF FIGURES

LIST OF ABBREVIATIONS

ASTM	American society for testing and materials
B10	commercial fuel, 10% vol biodiesel and 90% vol diesel blended fuel
B100	100% vol biodiesel
BSEC	brake-specific energy consumption
BSFC	brake-specific fuel consumption
BTE	brake thermal efficiency
CLD	chemiluminescence detector
CO	carbon monoxide
CO_2	carbon dioxide
CPSI	cells per square inch
CVS	constant volume sampler
D	dry mass
DOC	diesel oxidation catalyst
DPF	diesel particulate filter
ECU	engine control unit
EDS	energy dispersive X-ray spectroscopy
EGR	exhaust gas recirculation
EGT	exhaust gas temperature
EUDC	extra-urban driving cycle
EV	electric vehicle
F-DPF	full-flow diesel particulate filter
FID	flame ionization detector
HC	hydrocarbon
IF	inorganic fraction
ISO	international organization for standardization
M	saturated mass
$\dot{m}_f$	fuel flow rate
M_i	emission factor of pollutant i
N	engine speed
NDIR	non-dispersive infrared

(Continued)

NEDC	new European driving cycle
NO	nitric oxide
NO_2	nitrogen dioxide
NOx	nitrogen oxides
N_p	particulate number emission factor
O_2	oxygen
OBD	on-board diagnosis
P	apparent porosity
P-CDPF	partial-flow catalyzed diesel particulate filter
PM	particulate matter
PN	particulate number
ppm	parts per million
$\dot{Q}_{in}$	input energy
Q_{LHV}	lower heating value
rpm	revolutions per minute
S	suspended mass
SEM	scanning electron microscopy
SO_2	sulfur dioxide
SOF	soluble organic fraction
T	engine torque
THC	total hydrocarbon
UDC	urban driving cycle
ULSD	ultra-low sulfur diesel
V	exterior volume
V_{IP}	volume of impervious portion
V_{OP}	volume of opened pores
$\dot{W}_{b\ (kW)}$	brake power
ρ_{water}	water density

CHAPTER 1
INTRODUCTION

1.1 Background

The environmental and health impacts of vehicular emissions have become significant concerns globally. Internal combustion engines emit substantial amounts of harmful gaseous pollutants such as nitrogen oxides (NOx), carbon monoxide (CO), hydrocarbons (HC), and particulate matter (PM) [1]. These emissions contribute to air pollution, smog formation, and pose serious health risks, including respiratory and cardiovascular diseases [2,3]. The diesel combustion process is inhomogeneous, with fuel being directly injected into the combustion chamber at the end of the compression stroke, resulting in the production of a large amount of particulate matter (PM). Diesel engine emits PM at rates six to ten times higher than gasoline engine [4]. However, despite this drawback, diesel engine is one of the most fuel-efficient and thermally efficient internal combustion engines and has been widely employed in various types of road transportation.

With the increasing recognition of climate change and air quality issues, there has been a notable shift towards electric vehicles (EVs) as a cleaner and more sustainable alternative to traditional internal combustion engine vehicles [5]. Electric vehicles produce zero tailpipe emissions, thereby reducing the environmental and health impacts associated with vehicular emissions. Governments and policymakers worldwide are implementing initiatives to promote the adoption of EVs, including financial incentives, infrastructure development, and stricter emission regulations [6]. However, the transition to EVs is a gradual process, and many older, untreated vehicles continue to operate on roads beyond their lifespan in many developing countries, emitting harmful pollutants.

Diesel Particulate Filters (DPF) and biodiesel have emerged as promising technologies and alternative fuels, respectively, to mitigate the adverse effects of diesel emissions. DPFs are designed to trap and remove particulate matter from the exhaust gases, thereby reducing PM emissions. On the other hand, biodiesel, which is produced from renewable sources such as vegetable oils and animal fats, has been

shown to produce lower levels of harmful emissions compared to conventional diesel [7,8].

Despite the potential of DPF and biodiesel in reducing emissions, there is limited research focusing on their combined use, especially in older, untreated diesel vehicles commonly found in many developing countries. These vehicles often lack modern emission control technologies and are significant contributors to urban air pollution. Therefore, there is an urgent need to explore effective and practical solutions to reduce emissions from these vehicles and improve urban air quality.

1.2 Objectives

This research aims to investigate the effectiveness of using a ceramic-based P-DPF in conjunction with biodiesel to reduce harmful gaseous and particulate matter emissions from older, untreated diesel vehicles. The findings of this research could provide valuable insights for policymakers, vehicle owners, and the automotive industry in implementing effective emission reduction strategies. The following objectives are included in this thesis:

1) To investigate the microstructure of a ceramic-based partial-flow diesel particulate filter (P-DPF).
2) To evaluate the impacts of a ceramic-based P-DPF on vehicle performance and emission characteristics under steady-state conditions.
3) To evaluate the effectiveness of a ceramic-based P-DPF in reducing regulated emissions under the new European driving cycle.

1.3 Scope of Work

This research is conducted on an untreated light-duty diesel vehicle powered by a 2.5-liter engine. The research comprises three main sections: examining the microstructure of the P-DPF substrate, evaluating the impacts of P-DPF on vehicle performance and emission characteristics under steady-state engine conditions, and investigating the effectiveness of P-DPF in reducing regulated emission under the new European driving cycle. The details of this research are as follows:

1) Microstructure properties of P-DPF, including wall thickness, channel width, coating layer, pore fraction, pore size, and elemental compositions of the substrate and catalyst, are inspected by scanning electron microscopy (SEM), energy dispersive

X-ray spectroscopy (EDS), and ImageJ software. The porosity of P-DPF is determined by Archimedes method following standard ASTM C373-88.

2) Impact of P-DPF on the vehicle is evaluated by measuring the fuel flow rate at several steady-state conditions, engine speeds of 1500, 2000, and 2500 rpm, and loads of 84, 112, 140, and 160 Nm using commercial fuel B10 and biodiesel B100. Fuel flow rate, brake-specific fuel consumption, brake-specific energy consumption, input energy, and brake thermal efficiency are derived for the evaluation. The effect of P-DPF on exhaust emissions is also investigated by collecting exhaust emission, smoke intensity, exhaust gas temperature, and pressure drop before and after P-DPF.
3) The effectiveness of P-DPF in reducing regulated emissions from vehicle exhaust is assessed by examining emission factors of these pollutants under NEDC. The feasibility of retrofitting in older and untreated diesel vehicles is also discussed.

CHAPTER 2

LITERATURE REVIEW

2.1 Diesel Engine Emission Characteristics

The complete combustion of diesel fuel for ideal thermodynamic equilibrium generates carbon dioxide (CO_2) and water (H_2O) [9]. However, actual diesel combustion is not an ideal process for several reasons, such as the air-fuel ratio, combustion temperature, ignition timing, turbulence in the combustion chamber, and air-fuel concentration. Therefore, byproducts like CO, HC, SO_2, NOx, and PM are also produced. NOx constitutes the highest proportion of harmful diesel emissions, with a rate of more than 50%, followed by PM. The concentration of CO and HC is minimal as diesel engine is a lean combustion engine. Besides, a minimal amount of SO_2 is included in pollutant emissions due to the sulfates contained in the fuel, depending on its quality. Most oil distributors and customers nowadays prefer ultra-low sulfur diesel (ULSD) to prevent the adverse effects of SO_2. Although the harmful pollutants contribute less than 1% to the total composition of diesel exhaust, a large number of diesel vehicles on the road nowadays emphasizes a critical issue [10,11].

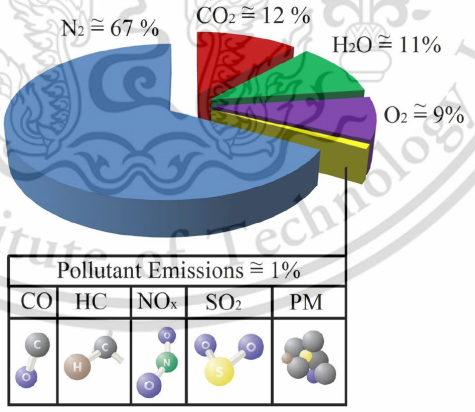

Figure 2.1 Diesel exhaust gas compositions [4]

2.1.1 Formation of Gaseous Emissions

Carbon monoxide (CO) is generated during incomplete combustion when the oxidation process is not fully completed. A significant factor contributing to the concentration of CO is the excess air-fuel ratio or lambda, with the highest levels

observed when lambda is less than 1, indicating a rich mixture [12]. Despite diesel engines primarily operating on lean combustion, a rich mixture is required during starting and acceleration. In these conditions, not all the carbon can be converted to CO_2 due to air deficiency, leading to the formation of CO. Additionally, a small amount of CO is produced under lean conditions due to chemical kinetic effects [13].

Hydrocarbons (HC) are unburned fuels due to inadequate temperatures near the cylinder wall. At this location, the temperature of the air-fuel mixture is notably lower than at the center of the cylinder [14]. Diesel hydrocarbon emissions mainly occur at light loads, with lean air-fuel mixing being the primary source of these emissions. In lean mixtures, the flame speeds can be too slow for complete combustion during the power stroke, or combustion may not occur at all, leading to increased hydrocarbon emissions [15].

The main factors influencing the formation of nitrogen oxides (NOx) are temperature and oxygen concentration. When the in-cylinder temperature exceeds 1600°C, nitrogen (N_2) reacts with oxygen (O_2) to produce NOx via the Zeldovich mechanism [16]. The quantity of NOx produced depends on the temperature in the cylinder, the concentration of reactants, and the residence time [17]. NOx consists mainly of nitric oxide (NO) and nitrogen dioxide (NO_2), with NO making up 85-95% of the total. In the atmosphere, NO is gradually transformed into NO_2. In the post-treatment systems, NO_2 is preferred to O_2 as the oxidizing gas for soot oxidation due to its lower temperature requirement.

2.1.2 Formation of Particulate Matter

2.1.2.1 Formation Process

Soot formation from hydrocarbons in the vapor phase to solid soot particles encompasses six key processes: pyrolysis, nucleation, coalescence, surface growth, agglomeration, and oxidation [18]. These processes are depicted schematically in **Figure 2.2**. The oxidation process, which transforms hydrocarbons into CO, CO_2, and H_2O, can occur at any stage. Fuel pyrolysis is a process in which fuel undergoes a change in molecular structure at high temperatures in the absence of sufficient oxygen. This process produces specific species that serve as precursors or building blocks for soot. The rate of this transformation depends on temperature and concentration and

is generally endothermic. Nucleation involves the formation of particles from gas-phase reactants with diameters ranging from 1.5-2 nm, referred to as nuclei. Surface growth involves the addition of mass to the surface of a nucleated soot particle. During this phase, the hot reactive surface of the soot particles readily interacts with gas-phase hydrocarbons. This interaction increases soot mass while the particle count remains consistent. The majority of the soot mass is accumulated during surface growth, making the duration of this process crucial in determining the total soot mass or soot volume fraction. Coalescence occurs when particles collide and coalesce, reducing the particle count while maintaining the combined mass of the two soot particles. Agglomeration takes place when individual or primary particles adhere together to form larger groups of primary particles. These primary particles typically range from 20-70 nm, depending on the operating conditions, injector type, and injection conditions [19-22]. Following combustion, the aggregate particles range from 100 nm to 2 μm and are observed to form chain-like or clumped structures [23].

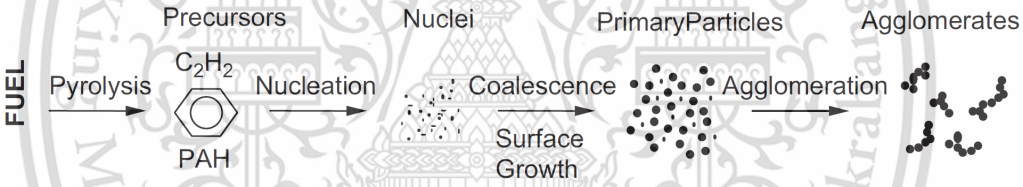

Figure 2.2 Soot formation process [18]

Figure 2.3 displays the size distribution of PM mass and PN from diesel exhaust, classified into nucleation mode, accumulation mode, and coarse mode based on the aforementioned formation processes. A notable concern is that, while the majority of PM mass exists in the accumulation mode with diameters ranging from 0.1-0.3 μm, over 90% of particles from diesel engine are in nucleation mode with diameters between 5-50 nm [24]. Considering by number, most of the particles emitted from diesel engine are nanoparticles.

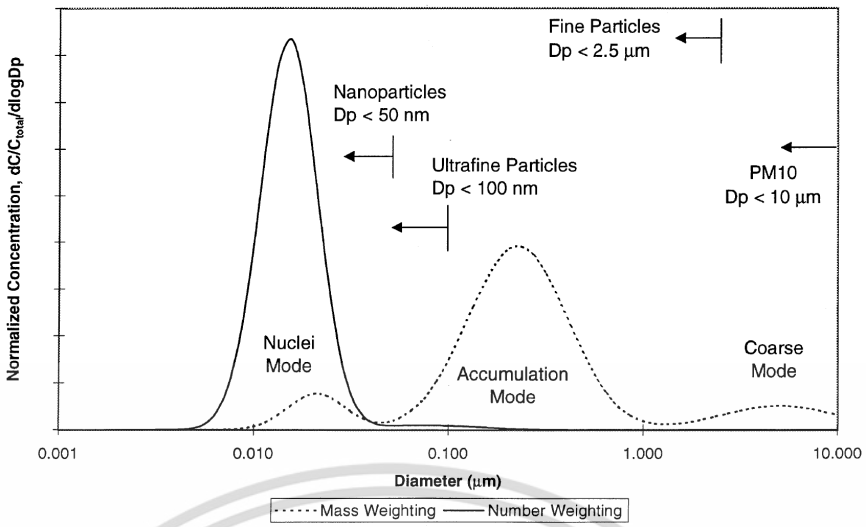

Figure 2.3 Size distribution of particulate mass and particulate number [24]

2.1.2.2 Elemental Composition of Particulate Matter

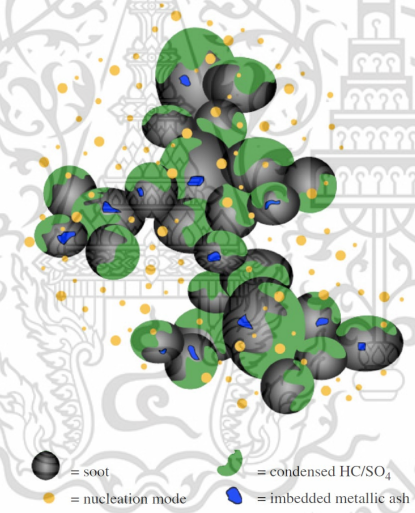

Figure 2.4 Conception of diesel PM [25]

Particulate matters (PM) in exhaust gas are generated during the combustion process. They result from the aggregation of extremely fine particles that stem from the incomplete combustion of hydrocarbons in the fuel and lube oil. These particles are comprised partly of burned fuel, burned lube oil, fuel oil ash content, cylinder lube oil, sulfates, and water [25]. In a transient test using a heavy-duty diesel engine, Kittelson [24] indicated that the typical particle composition is 41% carbon, 7% unburned fuel, 25% unburned oil, 14% sulfate and water, and 13% ash and other components. PM can be categorized into three primary components: soot, soluble

organic fraction (SOF), and inorganic fraction (IF). Approximately 50% of the total PM is soot, which appears as black carbon. SOF comprises heavy hydrocarbons that are absorbed or condensed onto the soot, originating partly from lubricating oil, unburned fuel, and other compounds produced during combustion. SOF levels are highest at light engine loads when exhaust temperatures are low. The IF is primarily composed of ash derived from metals associated with engine wear and lubricants.

2.2 Biodiesel Emission Characteristics

Biodiesel offers a practical solution for reducing particle emissions with minimal or no need for engine modifications [7,8]. It presents numerous benefits as an alternative to conventional diesel fuel, mainly due to its renewable feature. These benefits include low sulfur and aromatic content, a higher flash point, better lubricity, an increased cetane number, and non-toxicity. Nonetheless, biodiesel has its limitations, including higher viscosity, an increased pour point, a reduced heating value, and decreased volatility [26-29].

Numerous studies have investigated the impact of biodiesel on diesel engines, with a focus on combustion, emissions, and performance. Buyukkaya [30] examined the effects of neat rapeseed oil and its blends, up to 70%, on the performance, emissions, and combustion of a diesel engine. The findings revealed that B20 offers the highest brake thermal efficiency (BTE) and could be a potential solution for unmodified diesel engines. The use of biodiesel resulted in lower smoke opacity and higher NOx emissions compared to standard diesel fuel. Biodiesel also showed higher brake-specific fuel consumption (BSFC) at maximum torque and rated power than diesel fuel. Additionally, biodiesel and its blends exhibited shorter ignition delays due to their higher cetane numbers. This observation aligns with the research by Nguyen et al. [31], which indicated that the cetane number of pure biodiesel is approximately 30% higher than that of fossil fuel-derived diesel. This difference can be attributed to the increased oxygen content in biodiesel.

Canakci [32] proposed that the exhaust temperature for biodiesel is lower than that for diesel fuel, suggesting earlier combustion and a longer expansion period. Furthermore, biodiesel demonstrated a significant reduction in unburned HC, CO, and PM, while NOx emissions increased by 11.2%. In a study conducted by Can [33] using

a single-cylinder diesel engine fueled with waste cooking oil biodiesel blends at four different engine loads, it was observed that the addition of biodiesel resulted in a shorter ignition delay and earlier combustion timings due to its higher cetane number. This led to a slight decrease in the maximum heat release rate and the rate of pressure rise within the cylinder, while generally prolonging the combustion duration.

2.3 Current Diesel Emission Control Technology

Biodiesel serves as an advantageous alternative fuel to mitigate toxic emissions from diesel vehicles. Nevertheless, due to increasingly strict emission regulations, automotive manufacturers have implemented various strategies that target both the combustion and post-combustion stages. In the combustion stage, efforts are made to enhance advanced combustion through the use of the common rail direct injection system, where fuel is directly introduced into the combustion chamber, and by employing the exhaust gas recirculation (EGR) system. The EGR system reduces NOx emissions by recirculating a portion of exhaust gas back into the combustion chamber. While these new technologies have notably improved combustion efficiency and decreased soot emissions, the necessity for after-treatment devices to meet regulatory emission standards persists. In the post-combustion stage, an after-treatment system, such as the diesel oxidation catalyst (DOC), is utilized to reduce CO and HC emissions [34], while the diesel particulate filter (DPF) is employed to trap and oxidize particulate matter through a regeneration process [35]. The combined use of DOC and DPF is also effective in reducing both gaseous and particle emissions [36,37]. Furthermore, a catalyzed DPF can replace the aforementioned combination to address harmful pollutants [38].

2.3.1 Full-Flow Diesel Particulate Filter

The wall-flow DPF, also known as full-flow DPF (F-DPF), is comprised of a honeycomb-like substrate featuring parallel channels with internal porous walls separating each channel. As shown in **Figure 2.5**, these channels have alternatingly plugged inlet and outlet ends, directing exhaust gas to flow through the porous walls. F-DPF can achieve a filtration efficiency exceeding 99% [39]. Smaller mean pore sizes in the walls enhance both efficiency and backpressure [40]. However, as the F-DPF becomes saturated with PM, it restricts exhaust flow, causing an increase in

backpressure [41]. This rise in backpressure is the main factor behind diminished engine performance, notably affecting fuel flow rate and thermal efficiency [42,43]. To prevent backpressure buildup, it is essential to regularly remove the accumulated ash. The trapped PM must be oxidized by raising the temperature within the filter through a regeneration process. Active regeneration can be achieved by using an external heat source like a burner or by periodically injecting fuel into the combustion chamber at a later stage, a method known as active regeneration [44].

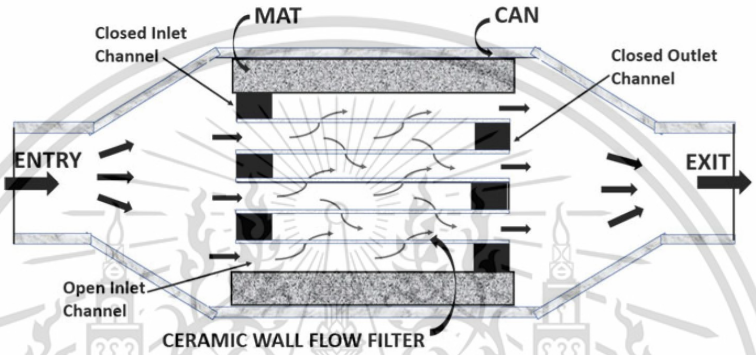

Figure 2.5 Schematic diagram of F-DPF [45]

2.3.2 Partial-Flow Diesel Particulate Filter

The schematic diagram of metallic partial-flow DPF (P-DPF) is shown in **Figure 2.6**. The P-DPF is composed of multiple layers of metal guide foil and fibrous fiber media. These are arranged in stacks within the filter. The corrugated foils form ducts that taper into trapezoidal shapes. Tapered ends on opposite sides of the filter media create a dynamic pressure gradient, guiding the exhaust flow through the filtering material. The metal foil directs a portion of the vehicle's exhaust flow towards the metal filtering media, effectively capturing PM. The filter can also be coated with a catalyst to aid in converting absorbed HC and CO into CO_2 and water. Furthermore, it promotes soot oxidation by utilizing NO_2 and O_2 to transform soot into CO_2. The concentration of NO_2 is increased by converting NO in the exhaust to NO_2, assisted by the catalyst. Because of its flow-through properties, P-DPF enables exhaust flow to bypass when saturated with soot and ash, preventing clogging. This design leads to lower filtration efficiency and reduced backpressure compared to F-DPF, with an efficiency of approximately 50% [46].

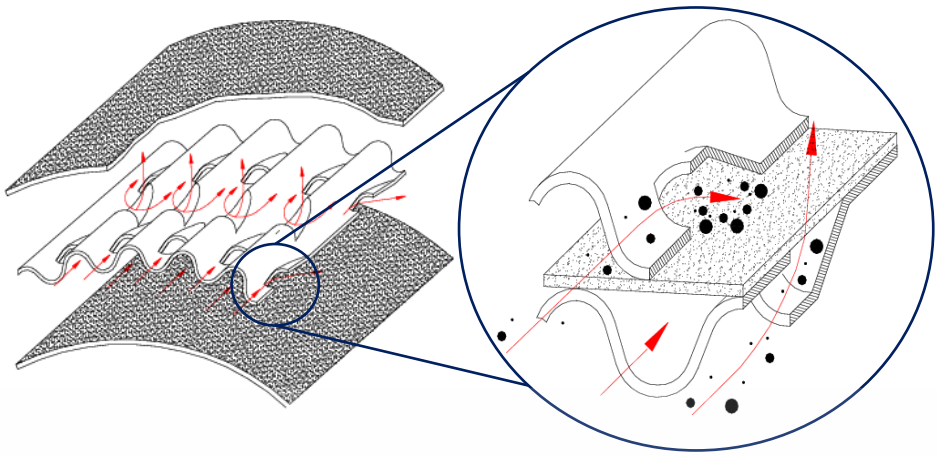

Figure 2.6 Schematic diagram of partial-flow diesel particulate filter (P-DPF) [47]

Several studies have explored the effectiveness of P-DPF in trapping PM and facilitating passive regeneration across various diesel engine setups. In a study by Isaline et al. [48], an uncoated P-DPF was utilized in a light-duty engine to lower the frequency of active regeneration in full-flow DPF (F-DPF) under different engine conditions. The study revealed that P-DPF alone reduced PM mass and PN by more than 25%. When integrated into the system, there was a 30% reduction in PM mass within the F-DPF. This reduction led to a more gradual and consistent pressure increase during the loading period, resulting in fewer regeneration events. Jacobs et al. [49] employed a DOC and P-DPF system to address PM and gaseous emissions in heavy-duty diesel vehicles. Their findings indicated a significant 74% reduction in PM for the new system and a 63% reduction for the aged system. Furthermore, CO and HC emissions were decreased by over 90%. The system maintained a consistent backpressure across various model years and exhaust temperature profiles, demonstrating its durability. In a related study, Kramer et al. [50] assessed the efficacy of a combined DOC and P-DPF system for off-highway diesel engines, focusing on PM reduction [43]. Their research showed a notable decrease of over 80% in stationary tests and more than 65% in transient tests without active regeneration. These results highlight the system's stability and efficiency under challenging conditions and extended low-temperature operation. This robust and passive solution represents a significant advancement in emission control systems for off-highway applications. According to research conducted by Mon Phyo et al. [51], there was a slight increase in exhaust backpressure when using P-DPF, leading to a minor rise in fuel flow rate and a decrease in thermal efficiency under

specific engine conditions. However, the installation did not significantly affect the overall results due to the very low backpressure. Additionally, particle emissions were passively oxidized by O_2 and NO_2, as indicated by measurements of O_2, NO, and CO_2 levels. These findings are consistent with the perspectives presented in the research by Oh et al. [52]. The installation of a long-catalyzed P-DPF without DOC in an untreated light-duty diesel vehicle was inspected by Dang et al. [53]. The authors stated that the catalyzed P-DPF reduced PN by 45% and PM mass by 60% when operating under the new European driving cycle. Furthermore, significant reductions of 48% in CO and 66% in total HC were also observed. This proposes a practical solution for reducing toxic pollutants from older diesel vehicles with minimal modifications.

CHAPTER 3

RESEARCH METHODOLOGY

This study investigates the effects of a catalytic partial-flow diesel particulate filter (P-DPF) on a light-duty diesel vehicle regarding fuel flow rate, brake thermal efficiency, and emission reduction characteristics utilizing commercial fuel B10 and biodiesel B100. The filter's microstructure is inspected by scanning electron microscopy to better understand the characteristics of its substrate. Subsequently, two test setups are conducted on chassis dynamometers: steady-state engine conditions and the new European driving cycle (NEDC) to compare the results with and without P-DPF. The initial test involves testing the vehicle to assess fuel flow rate, brake-specific fuel consumption, brake thermal efficiency, and exhaust emissions at three engine speeds: 1500, 2000, and 2500 rpm, corresponding to four loads: 84, 112, 140, and 160 Nm. The second test evaluates the emission factors of regulated emissions under the NEDC. The methodology overview of this research is illustrated in **Figure 3.1**.

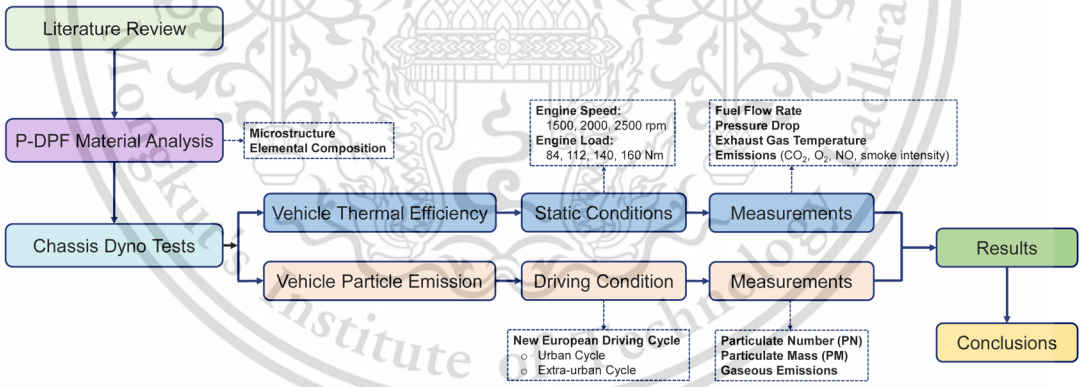

Figure 3.1 Methodology overview

3.1 Fuel Properties

Biodiesel provides the benefits of oxygenated fuel, improving combustion efficiency and decreasing harmful emissions [54]. In this research, commercial fuel B10 (containing 10% biodiesel) and pure biodiesel B100 (containing 100% biodiesel) are used. **Table 3.1** outlines the properties of these fuels. Compared to B10, B100 has a lower carbon-to-hydrogen ratio, higher oxygen content, and a higher cetane number,

suggesting a potential solution to reduce smoke generation. Moreover, B10 has a higher net heating value and density than B100, indicating a negative correlation between heating value and biodiesel concentration in the blends.

Table 3.1 Fuel properties

Properties	Standards	B10	B100
Carbon (%wt)	ASTM D5291	84.66	76.73
Hydrogen (%wt)	ASTM D5291	13.56	12.45
Oxygen (%wt)	ASTM D5291	1.78	10.82
Lower heating value (MJ/kg)	ASTM D240	43.10	37.41
Cetane index	ASTM D967	54.9	-
Cetane number	ASTM D613	-	62.1
Fatty acid methyl ester	EN 14078	10.2 (%vol)	-
	EN 14103	-	98.1 (%wt)
Density @ 15^{0}C (kg/m^{3})	ASTM D4052	835	-
	ASTM D1298	-	875
Viscosity @ 40^{0}C (mm^{2}/s)	ASTM D445	3.0	4.5
Distillation (^{o}C)	ASTM D86-11b		
T10		180	336.2
T90		344.2	352.3

3.2 Vehicle Specifications

This study focuses on a commercial light-duty diesel vehicle, with the specifications listed in **Table 3.2**. The vehicle is equipped with a 2.5-liter direct injection 4-stroke diesel engine, complemented by a turbocharger. This engine delivers a maximum power of 75 kW at 3600 rpm and generates a peak torque of 260 Nm ranging from 1600 to 2400 rpm. Except for an external fuel tank, the fuel supply system remains unaltered in the test vehicle. The vehicle performance, emission characteristics, and fuel efficiency are evaluated under various driving conditions to assess its overall performance and environmental impact.

Table 3.2 Vehicle specifications

Items	Details
Type of vehicle	Light-duty diesel vehicle
Vehicle mass	1590 kg
Engine model	2KD-FTV, inline four-cylinder
Fuel system	Common rail direct injection
Air intake system	Turbocharged
Displacement volume	2494 cc
Bore x Stroke	92.0 mm x 93.8 mm
Compression ratio	18.5:1
Maximum power	75 kW @ 3600 rpm
Maximum torque	260 Nm @ 1600 - 2400 rpm

3.3 Ceramic Partial-Flow Diesel Particulate Filter

Figure 3.2 shows the macroscale design of the ceramic catalyzed partial-flow diesel particulate filter (P-DPF) utilized in this research. The filter is structured with a honeycomb substrate composed of several square channels. The inlet channels are entirely open, whereas the outlet channels are alternately clogged. This design allows some of the exhaust gas to pass through without being filtered while the rest is forced to flow through the porous walls for filtration, as depicted in **Figure 3.3(a)**. Compared to the F-DPF, this design reduces backpressure but lowers filtration efficiency. The filtration behavior of the wall-flow filtering mechanism is shown in **Figure 3.3(b)**. Initially, soot clogs the pores, causing the filtration efficiency and pressure drop to increase. Subsequently, soot accumulation begins and forms a cake layer on the wall surface as the internal pore network is saturated. The substrate of P-DPF is coated with a catalytic material to facilitate the conversion of CO and HC into CO_2 and H_2O. Additionally, the catalyst aids in increasing the NO_2/NOx ratio in the exhaust gas by oxidizing NO to NO_2 since it is preferable for the passive oxidation of soot at exhaust gas temperatures above 250°C. In the test vehicle, the P-DPF is positioned downstream of the turbocharger to utilize the hot exhaust gas, as seen in **Figure 3.3(b)**. Detailed parameters of the filter can be found in **Table 3.3.** It has a cell density of 200 cells per square inch (CPSI) and dimensions of 200 mm in length and 144 mm in diameter.

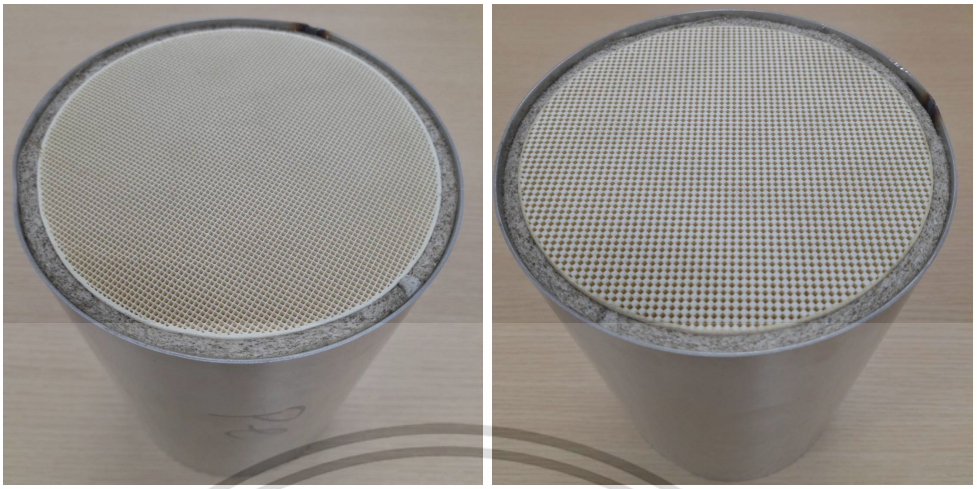

(a) open inlet channels (b) alternate clogged outlet channels

Figure 3.2 Ceramic partial-flow diesel particulate filter (P-DPF)

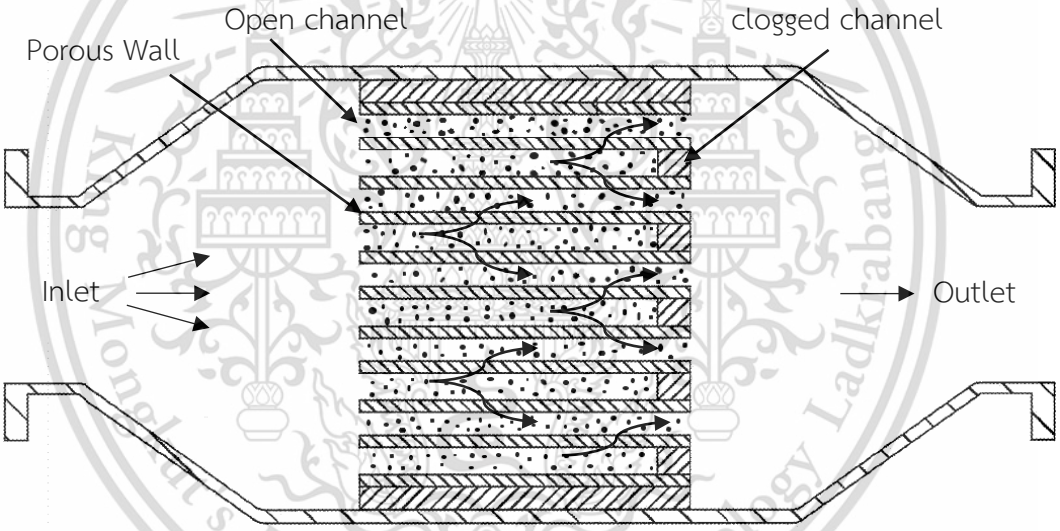

(a) schematic diagram of ceramic P-DPF

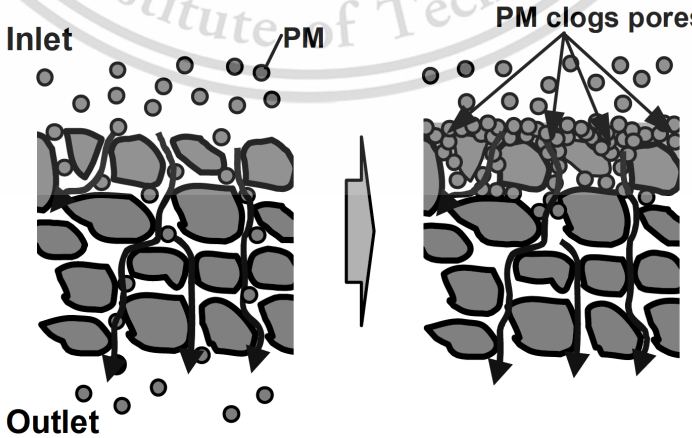

(b) filtration behavior of the wall-flow filtering mechanism [55]

Figure 3.3 Schematic diagram and filtration behavior of ceramic P-DPF

Table 3.3 Parameters of ceramic partial-flow diesel particulate filter (P-DPF)

Parameters	Values
Type of catalyst	ceria-zirconia oxide
Cell density (CPSI)	200
Length (mm)	200
Diameter (mm)	144
Porosity (%)	66
Mean pore size (μm)	14
Wall thickness (μm)	211

3.4 Research Methodology

3.4.1 P-DPF Microstructure Analysis

The microstructure of P-DPF is investigated using SEM (HITACHI S-3400N). A sample with 3 by 2 channels, as seen in **Figure 3.4**, is extracted from the P-DPF for inspection under various magnifications. Particularly, the structural parameters of the filter from the front view and side view, including wall thickness, channel width, and coating layer, are measured on SEM captures at 45x magnification with ImageJ software. The pore fraction of the filter substrate is also examined by selecting and polarizing an area of 100 μm x 100 μm from three SEM images at 750x magnification. Furthermore, the diameters of over 160 observed pores from the wall of P-DPF are measured to define pore size ranges and pore distributions. Afterwards, as illustrated in **Figure 3.5**, the elemental compositions of P-DPF substrate and catalyst are examined by selecting an area of interest at 1000x magnification for observation using energy dispersive X-ray spectroscopy (EDS). Based on the elemental composition, the substrate and catalyst components can be identified.

The experimental setups to identify the porosity of the P-DPF are shown in **Figure 3.6.** The porosity of P-DPF is determined using the Archimedes method, employing five specimens extracted from the monolithic filter following standard ASTM C373-88 [56]. Weights of the specimens are measured at each stage using the same digital scale (AND GF-400), accurate to 0.001 g. The dry mass (D) of the specimens is obtained after heating them to a constant mass in an oven. Subsequently, the specimens are boiled for 5 hours and then soaked in distilled water for an additional

24 hours. The suspended mass (S) of each specimen is determined while submerged in water, taking into account the varying water temperature and its density. Following the determination of the suspended mass, each specimen is gently blotted with a damp cloth to remove excess water from the surface, and the saturated mass (M) is measured. **Equations 3.1-3.4** are employed to calculate the apparent porosity of the samples based on the measured masses.

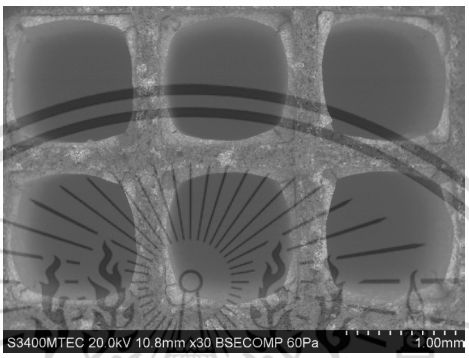

Figure 3.4 Sample from P-DPF inlet

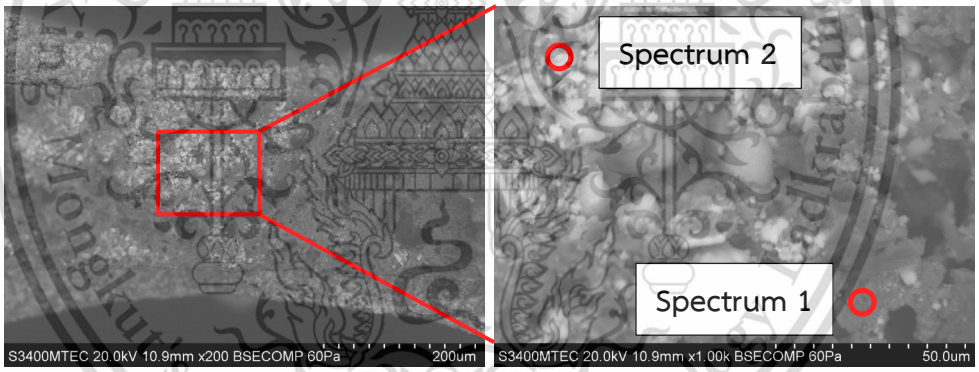

Figure 3.5 Selected areas for the elemental composition inspection

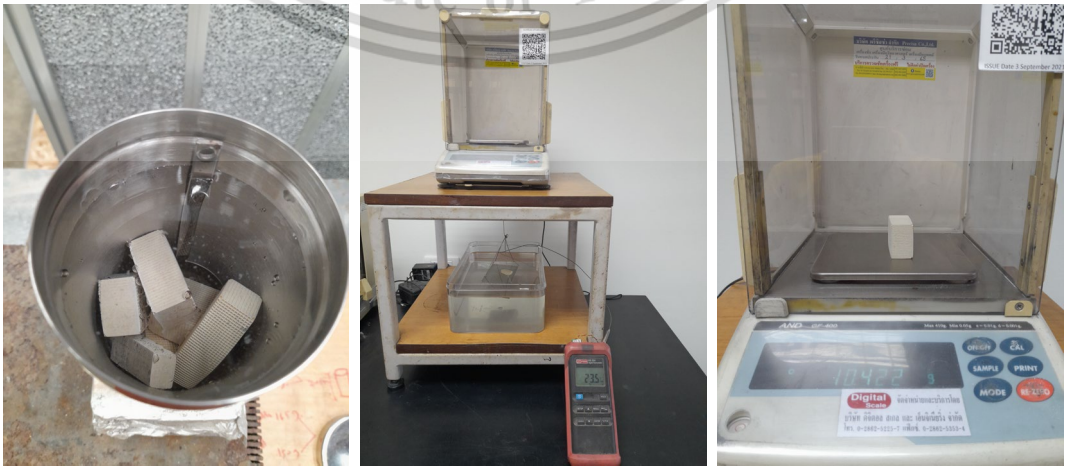

Figure 3.6 Setups for P-DPF porosity measurement

Volume of opened pores (cm^3):

$$V_{OP} = \frac{M - D}{\rho_{water}} \quad (3.1)$$

Volume of impervious portion (cm^3):

$$V_{IP} = \frac{D - S}{\rho_{water}} \quad (3.2)$$

Exterior volume (cm^3):

$$V = \frac{M - S}{\rho_{water}} \quad (3.3)$$

Apparent porosity (%):

$$P = \frac{M - D}{V} \times 100 \quad (3.4)$$

Where

M: saturated mass (g)

D: dry mass (g)

S: suspended mass (g)

ρ_{water}: water density (g/cm^3)

3.4.2 Thermal Efficiency and Emissions under Static Conditions

Figure 3.7 displays the experimental setup utilized to assess the effects of P-DPF on vehicle fuel flow rate, thermal efficiency, and emission characteristics. In this configuration, a light-duty diesel vehicle is placed on a chassis dynamometer, equipped with a cooling fan to mimic the air-cooled conditions of the radiator system. The engine speeds are fixed at 1500, 2000, and 2500 rpm and loads ranging from 84 to 160 Nm (30% to 60% of maximum engine torque) are adjusted via the accelerator pedal. An external fuel tank is linked to a weight scale (Jadever LGCN-1530) to determine fuel flow rate under specified conditions. To ensure result accuracy, the fuel flow rate for each condition is measured three times at 30-second intervals and averaged to determine the final values. The recirculated fuel is cooled by a cooling system to maintain a fuel temperature of 50°C. The Carman scan on-board diagnosis (OBD II) device is connected to the ECU to monitor engine coolant and fuel temperatures, confirming the vehicle is operating under normal conditions.

Exhaust gas temperature (EGT) and pressure drop are recorded for all test conditions to compare the differences with and without the installation of P-DPF.

Thermocouple (type K) and pressure sensor (MPX5050DP) are mounted on the exhaust pipe before and after the P-DPF location. The collected data is analyzed and visualized using Arduino software. These parameters are observed until stability is achieved within one and a half minutes for each condition, after which the steady-state values are recorded.

Exhaust from the vehicle is collected and measured to compare emissions with and without the introduction of P-DPF. Specifically, the exhaust gases are analyzed using a gas analyzer (AVL DITEST GAS 1000) to measure the fuel-air equivalent ratio, CO_2, O_2, and NO emissions. Additionally, a smoke meter (KOENG DS-2000R) equipped with a paper filter is used to assess the smoke intensity of the exhaust. The uncertainty of the measurements can be found in **Table 3.4**. To ensure accuracy, the measurements are repeated three times for each condition, and the results are averaged. The paper filter from the test condition with the highest smoke intensity is selected for observation under scanning electron microscopy (SEM).

Table 3.4 Uncertainty of measurements

Measurements	Uncertainty
Gas analyzer	
CO_2 (%)	±0.3%
NO (ppm)	±5 ppm
O_2 (%)	±0.02%
Pressure sensor (kPa)	±2.5%
Smoke meter (%)	±2%
Thermocouple (°C)	±2.2
Weight scale (g)	
AND GF-400	±0.001
Jadever LGCN-1530	±0.1

The vehicle brake power ($\dot{W}_b$), brake-specific fuel consumption (BSFC), brake-specific energy consumption (BSEC), and brake thermal efficiency (BTE) are calculated based on engine speed (N), torque (T), fuel flow rate ($\dot{m}_f$), fuel lower heating value (Q_{LHV}), and input energy ($\dot{Q}_{in}$) using the **equations 3.5-3.9** [57].

Brake power

$$\dot{W}_{b\ (kW)} = 2\pi NT \tag{3.5}$$

Brake-specific fuel consumption

$$BSFC_{\ (g/kWh)} = \frac{\dot{m}_f}{\dot{W}_b} \tag{3.6}$$

Brake-specific energy consumption

$$BSEC_{\ (kJ/kWh)} = \frac{\dot{m}_f}{\dot{W}_b}.Q_{LHV} \tag{3.7}$$

Input Energy

$$\dot{Q}_{in\ (kW)} = \dot{m}_f.Q_{LHV} \tag{3.8}$$

Brake thermal efficiency

$$BTE_{\ (\%)} = \frac{\dot{W}_b}{\dot{Q}_{in}} \tag{3.9}$$

Where

N: engine speed (rpm)

T: engine torque (N.m)

$\dot{m}_f$: fuel flow rate (g/s)

Q_{LHV}: lower heating value (kJ/g)

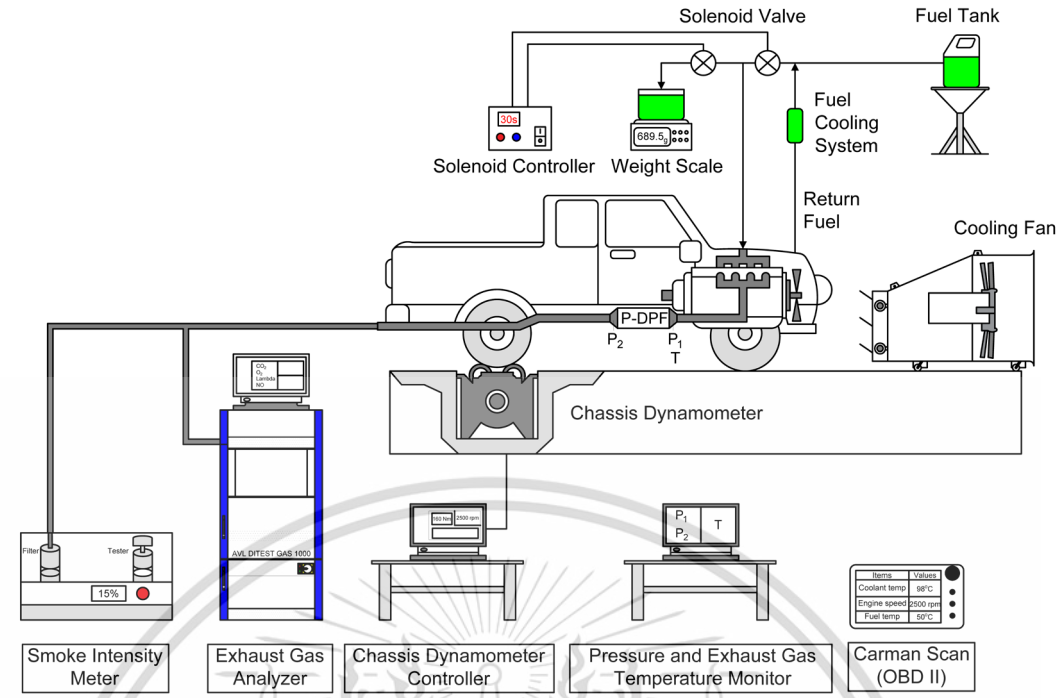

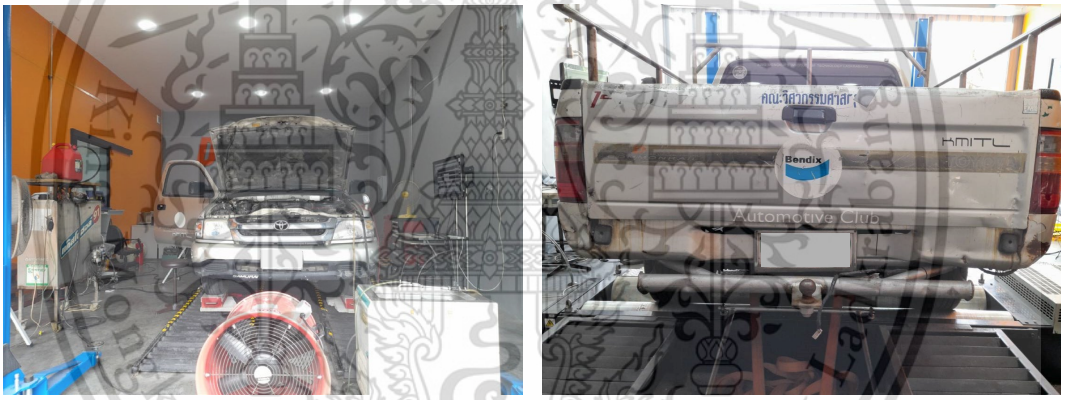

Figure 3.7 Schematic diagram and experimental setup for vehicle performance and emission testing under steady-state conditions

3.4.3 Emission Factors under the New European Driving Cycle

The emission factors for gaseous and particle pollutants from the examined vehicle are measured using the new European driving cycle (NEDC), as shown in **Figure 3.8**. This study is carried out at the Automotive Emission Laboratory, part of the Pollution Control Department of Thailand. The laboratory's testing system complies with the international standard ISO/IEC17025. The equipment specifications, testing procedures, and measurement accuracy adhere to UNECE regulations 83 and 101.

An inertial load is applied through a chassis dynamometer (Schenck Komeg EMDY 48) to replicate actual driving conditions. To ensure the accuracy of the measurements, the test room's temperature, humidity, and cooling fan are maintained

according to standard protocols. Moreover, an external fuel tank is used to minimize contamination from the primary fuel tank.

The driver's aid screen assists in maintaining the vehicle speed within NEDC specifications with a tolerance of 2 km/h. **Table 3.5** provides detailed information on the NEDC, which comprises the Urban Driving Cycle (UDC) and the Extra-Urban Driving Cycle (EUDC). In the UDC, four elementary cycles are combined to simulate the frequent cold-hot start characteristics typical of low engine load and low exhaust gas temperature (EGT) conditions in congested cities. These elementary cycles cover a total distance of approximately 4 kilometers in 780 seconds, with an average speed of 18.8 km/h. Following the UDC, the EUDC is implemented to represent a more aggressive, high-speed driving mode typical of highway conditions. During this cycle, nearly 7 kilometers are covered in 400 seconds, maintaining an average speed of 62.6 km/h.

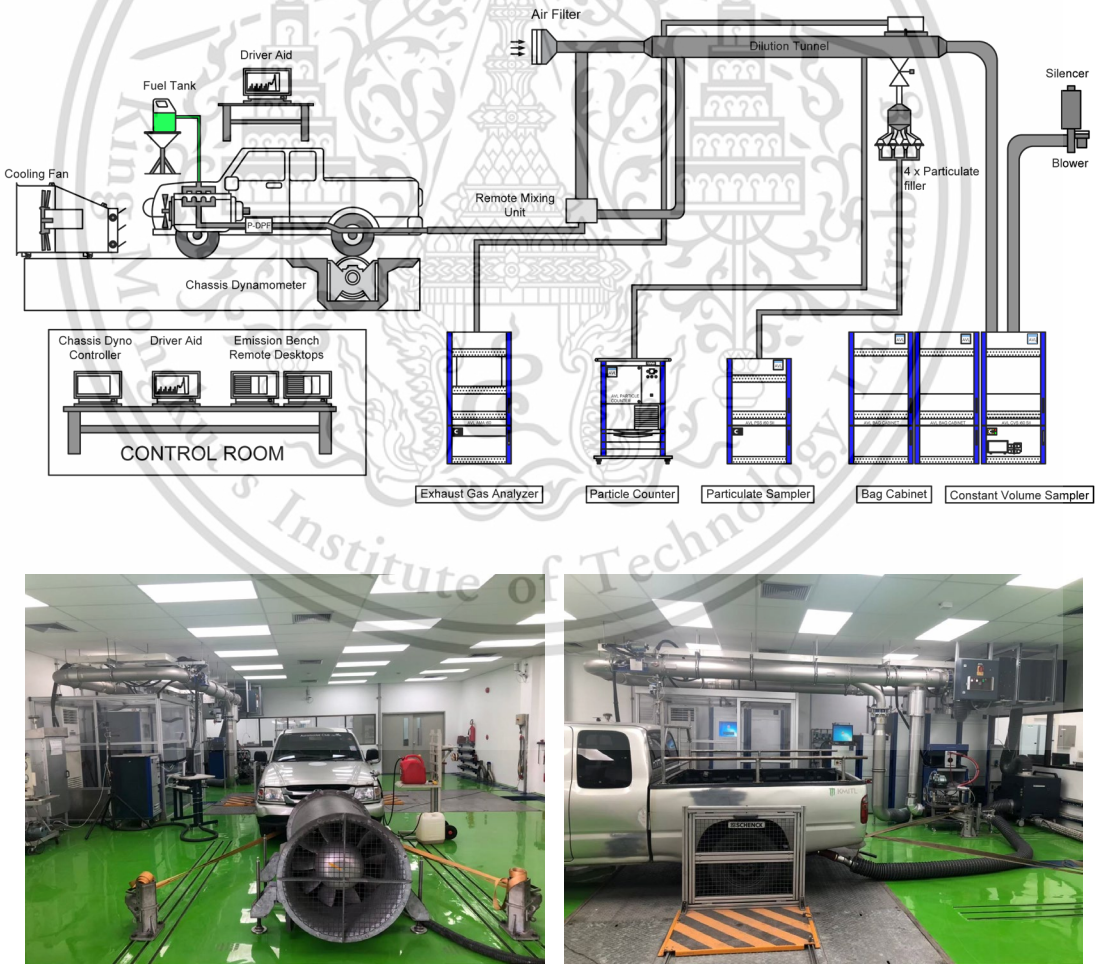

Figure 3.8 Schematic diagram and experimental setup for the regulated emission testing under the new European driving cycle (NEDC)

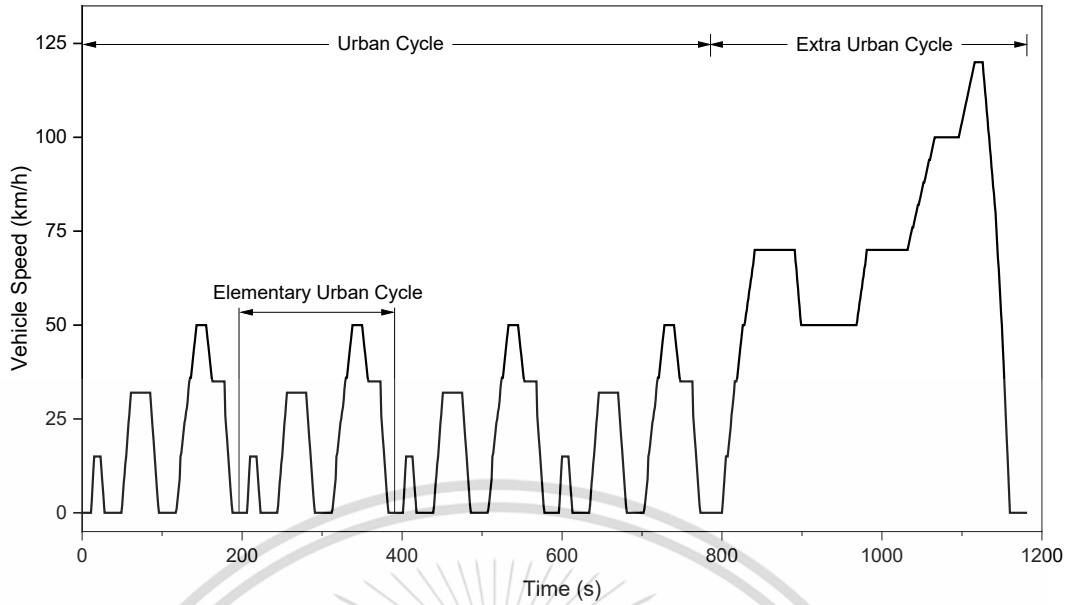

Figure 3.9 New European driving cycle

Table 3.5 Characteristics of the new European driving cycle

Details	Urban driving cycle	Extra-urban driving cycle
Distance (km)	4.067	6.956
Time (s)	780	400
Average speed (km/h)	18.8	62.6
Max speed (km/h)	50	120

The exhaust gas from the vehicle enters a dilution tunnel, where it combines with a precise amount of filtered ambient air from the surroundings. This process is designed to reduce the temperature, prevent condensation, and mimic the natural dispersion of exhaust that occurs in the atmosphere. The constant volume sampler (CVS) system maintains a uniform volume of diluted exhaust, which is then collected in a bag sampler to measure the concentration of pollutants in parts per million (ppm) for each cycle. The diluted exhaust is directed to gas analyzers to determine the real-time concentration of specific pollutants. The emission factor (g/km) for each pollutant in each cycle is calculated based on the concentration using **equation 3.10**. This study focuses on regulated emissions, specifically THC, CO, and NOx, utilizing the AVL AMA i60 gas analyzer. THC and NOx are analyzed using a flame ionization detector (FID) and

a chemiluminescence detector (CLD), respectively. CO emissions are detected using a non-dispersive infrared (NDIR) detector. Additionally, the gravimetric method, coupled with a particulate sampling system (PSS), is used to measure the particulate matter (PM) mass from the diluted exhaust. The filter is weighed at the beginning and end of each cycle, and the PM mass per covered distance is subsequently calculated. The particulate number (PN) concentration (#/cm³) is determined by a particle counter based on the light-scattering method. The PN emission factor (#/km) is then calculated from the concentration using **equation 3.11** for each driving cycle corresponding to the covered distance.

The emission factor of gaseous pollutants (g/km) is calculated from the real-time concentrations (ppm) by the following formula:

$$M_i = \frac{V_{mix} \times Q_i \times k_h \times C_i \times 10^{-6}}{d} \quad (3.10)$$

Where:

M_i: emission factor of pollutant i (g/km)

V_{mix}: volume of the diluted exhaust gas at standard conditions (273.2 K and 101.33 kPa), expressed in liter (l)

Q_i: density of pollutant i at 273.2 K and 101.33 kPa (g/l)

$$Q_{CO} = 1.25;\ Q_{HC} = 0.619;\ Q_{NOx} = 2.05$$

k_h: humidity correction factor for the calculation of mass emission of NOx

C_i: concentration of the pollutant i in the diluted exhaust gas (ppm)

d: distance corresponding to the operating cycle (km)

The emission factor of particulate number (g/km) is calculated from the real-time concentration (#/cm^3) by the following formula:

$$N_p = \frac{V \times k \times \bar{C}_s \times \bar{f}_r \times 10^3}{d} \quad (3.11)$$

Where:

N_p: particulate number emission factor expressed in particles per kilometer (#/km)

k: calibration factor to correct the particle number counter measurements to the level of the reference instrument where this is not applied internally within the

particle number counter. Where the calibration factor is applied internally within the particle number counter a value of 1 shall be used for k in the above equation

$\overline{C}_s$: corrected concentration of particles from the diluted exhaust gas expressed as the average particles per cubic centimetre figure from the emissions test including the full duration of the drive cycle

$\overline{f}_r$: mean particle concentration reduction factor of the volatile particle remover at the dilution setting used for the test

CHAPTER 4
RESULT AND DISCUSSION

4.1 Microstructural Analysis of P-DPF

4.1.1 Substrate Properties

Figure 4.1 shows SEM micrographs of the sample from P-DPF at various magnifications. The inlet of P-DPF is characterized by multiple open square channels while the outlet is identical to conventional wall-flow DPF with alternating clogged channels. A porous refractory layer to provide a high surface area for dispersion of catalytic metal is coated on the P-DPF substrate, which is essential for oxidation activity. Microscopic cracks and pores in this layer serve as pathways for exhaust gases and particles. Particles are trapped on the porous layer and wall through two filtration processes: deep-bed filtration and cake filtration [58]. In the early stage, the particles get trapped in the filter pores mainly due to interception and diffusion mechanisms. As deposition occurs within the filter wall, it alters the internal structure, affecting filtration efficiency. Once the structure reaches saturation and can not admit more particles, accumulation starts on the wall's surface, creating a cake layer. This stage is characterized by an increase in filtration efficiency and pressure drop.

Along with the wall pore size, wall thickness, channel width, and coating layer are among the parameters that affect the efficiency of a DPF. In this study, the measurements of these parameters are performed on SEM captures using ImageJ software. According to **Table 4.1**, the wall thickness ranges from 210 to 212 μm. Notably, while a thicker wall improves filtration efficiency, it also leads to increased pressure drop due to restricted passage. The channel width falls between 1200 and 1240 μm, with smaller channels corresponding to higher cell density in the filter. The coating thickness ranges from 38 to 129 μm, with a notably thicker washcoat present at the cell corners. On average, the dimensions for wall thickness, channel width, and coating layer are 211, 1220, and 63 μm, respectively.

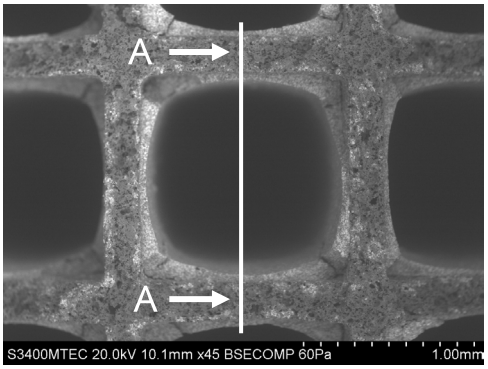

(a) open channels of P-DPF inlet

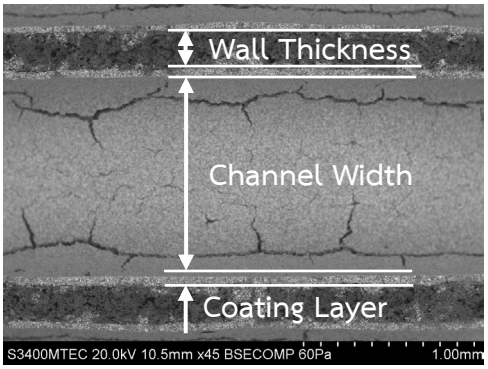

(b) cross-sectional view A-A

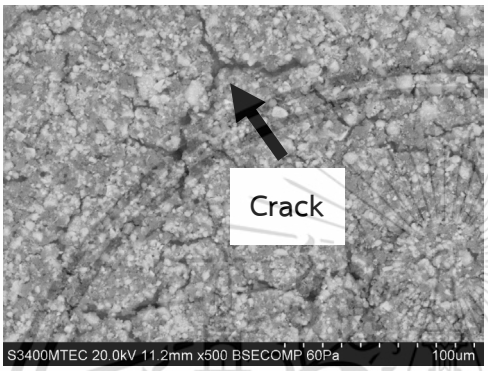

(c) surface of filter wall

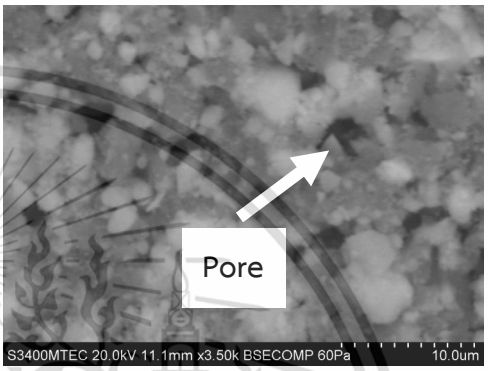

(d) closer observation of the filter wall

Figure 4.1 SEM micrographs of specimen extracted from P-DPF

Table 4.1 Measurements of P-DPF substrate properties

Number	Wall Thickness (μm)	Channel Width (μm)	Coating layer (μm)
1	210	1240	47
2	211	1210	42
3	212	1200	38
4	212	1200	129
5	212	1240	124
Average	211	1220	63

4.1.2 Elemental Composition

The substrate of P-DPF is characterized by ceramic-based material; its elemental composition is determined using energy-dispersive X-ray spectroscopy (EDS). Furthermore, components of the catalyst coated on the P-DPF substrate are also examined. **Figure 4.2** indicates the EDS spot analysis of the P-DPF substrate and catalyst, focusing on small areas of interest on the specimen's surface. The analysis reveals the presence of oxygen (O_2), magnesium (Mg), aluminum (Al), and silicon (Si) as

major elements of the substrate, while other elements are identified as catalyst and inclusions. **Table 4.2** summarizes the elemental compositions of the tested specimen from EDS analysis, with O_2, Si, Al, and Mg contributing weights of 34%, 26%, 23%, and 8%, respectively. Based on the findings and supporting results from previous research [59,60], it is suggested that P-DPF substrate primarily consists of the main constituents in the production of cordierite, characterized by chemical formula 2MgO.2Al2O3.5SiO2 named magnesium aluminum silicate. The primary components identified in the catalyst are zirconium (Zr), cerium (Ce), and O_2, making up approximately 30%, 28%, and 20%, respectively. This suggests that the catalyst material is a ceria-zirconia oxide. This mixed oxide offers enhanced thermal stability against sintering, improved physicochemical characteristics, reduced oxidation enthalpies, and a higher oxygen storage capacity compared to individual oxides [61].

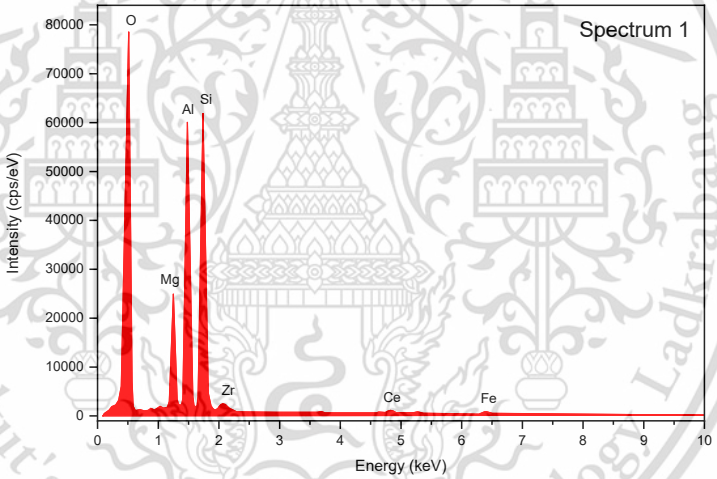

(a) elemental composition of the substrate

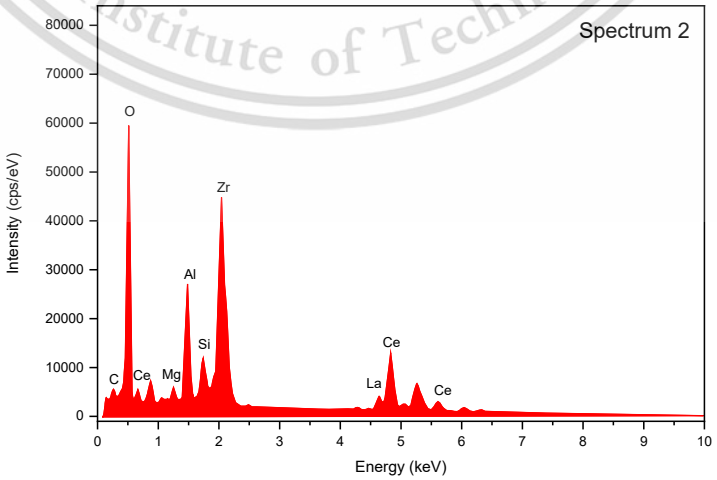

(b) elemental composition of the catalyst

Figure 4.2 Elemental compositions of P-DPF substrate and catalyst

Table 4.2 Elemental compositions of P-DPF substrate and catalyst from EDS analysis

Elements	Substrate (%wt)	Catalyst (%wt)
O	34.17	20.05
Si	26.14	2.83
Al	23.22	7.01
Mg	8.55	1.29
Ce	4.65	28.41
Zr	1.75	29.62
Fe	1.52	-
La	-	6.84
C	-	3.95

4.1.3 Porosity and Pore Size Profile

Archimedes method is performed to define the porosity of P-DPF substrate with five specimens extracted from the monolithic filter following standard ASTM C373-88. The dry mass (D) of specimens is collected after heating up in the oven to a constant mass. Afterwards, specimens are boiled for 5 hours and soaked for 24 hours in distilled water. Suspended mass (S) of each specimen is determined while suspended in water. After determining the suspended mass, blot each specimen slightly with a moistened linen to remove excess water from the surface and measure the saturated mass (M). The results of the porosity measurement for each specimen are presented in **Table 4.3**. According to the results, the average apparent porosity of all specimens is approximately 66%, with negligible deviations for each specimen. This result is comparable to the findings from some other studies [62,63].

Table 4.3 Measurements of porosity for P-DPF specimens

Number	Dry mass (g)	Suspended mass (g)	Saturated mass (g)	Porosity (%)
Specimen 1	10.422	7.051	17.121	66.5
Specimen 2	9.374	6.322	15.361	66.2
Specimen 3	8.704	5.913	14.224	66.4
Specimen 4	7.267	4.929	11.909	66.5
Specimen 5	5.624	3.792	9.191	66.1
Average	-	-	-	66.3

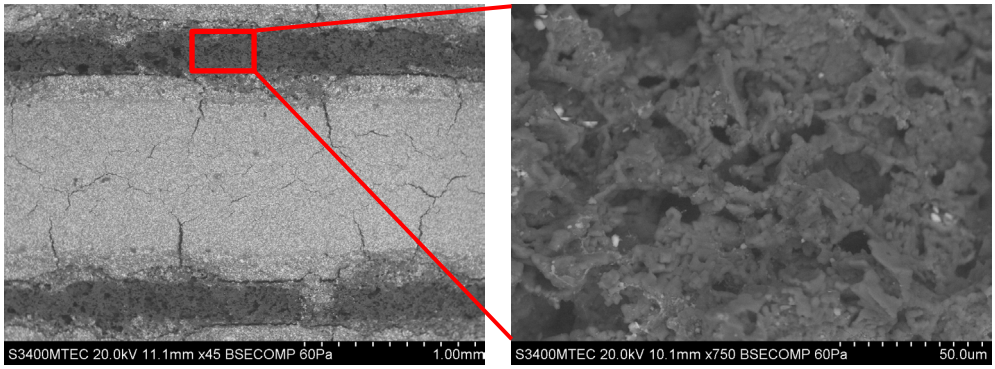

a) high-magnification images of P-DPF wall

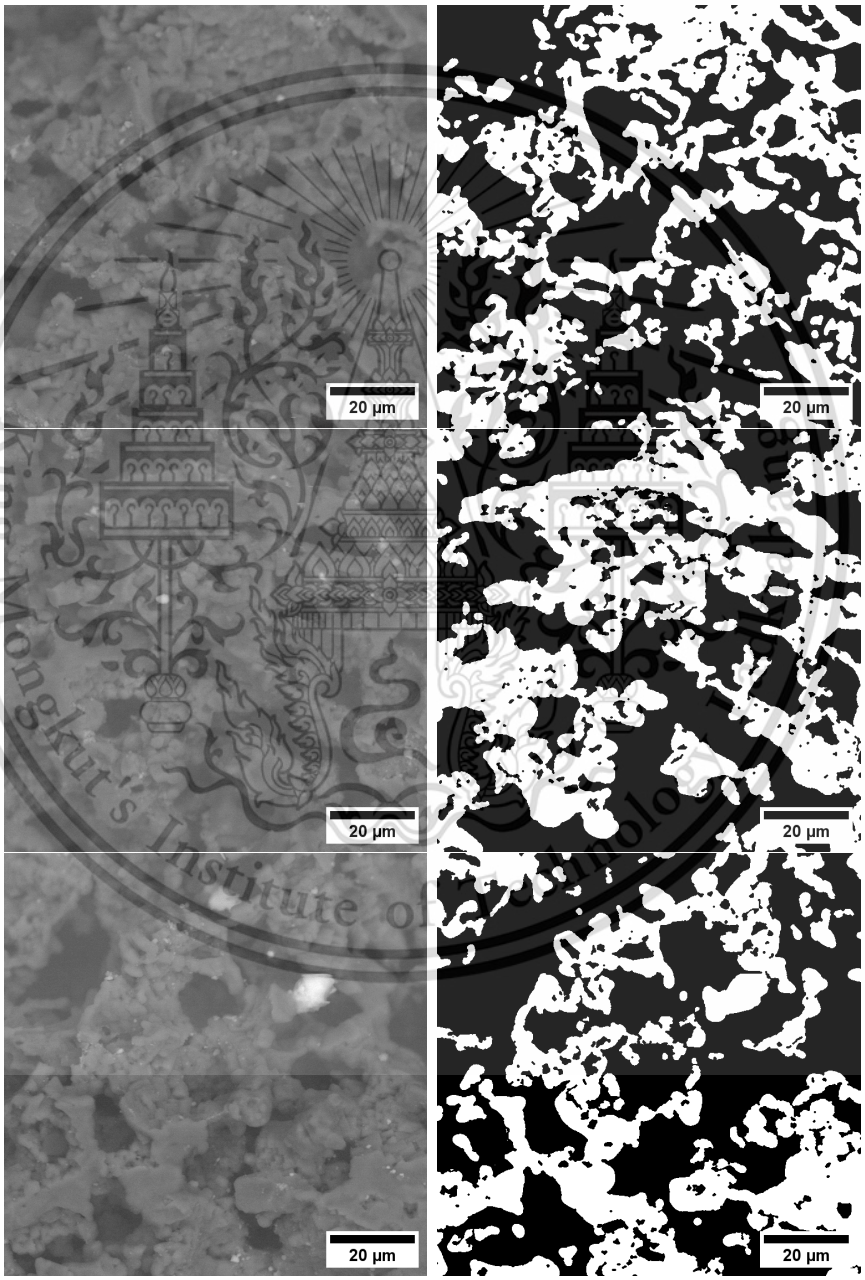

(b) analyzed images of the P-DPF wall surface

Figure 4.3 Pore fraction analysis of P-DPF substrate using ImageJ software

Figure 4.3 shows the SEM micrograph of the P-DPF wall, with a closer observation of its surface at 750x magnification. Three 100 µm x 100 µm sections at different wall surface positions were used to measure the pore fraction using ImageJ software. The processed image displays black and white regions, where the black areas represent the pores and the white areas indicate the substrate. The results in **Table 4.4** show that pores occupy approximately 58%, 54%, and 61% of three analyzed images, with an average pore fraction of 58%. Furthermore, the microstructure of the filter is examined through the pore size. A total of 162 observed pores are measured using ImageJ software. **Figure 4.4** indicates the distribution of pore sizes in the P-DPF wall, with pores ranging from 3 to 47 µm. More than 80% of pore diameters fall between 3 and 20 µm, indicating a mean pore size of 14 µm.

Table 4.4 Results of the pore fraction analysis of the P-DPF substrate

Sample	Porosity (%)
Image 1	58
Image 2	54
Image 3	61
Average	58

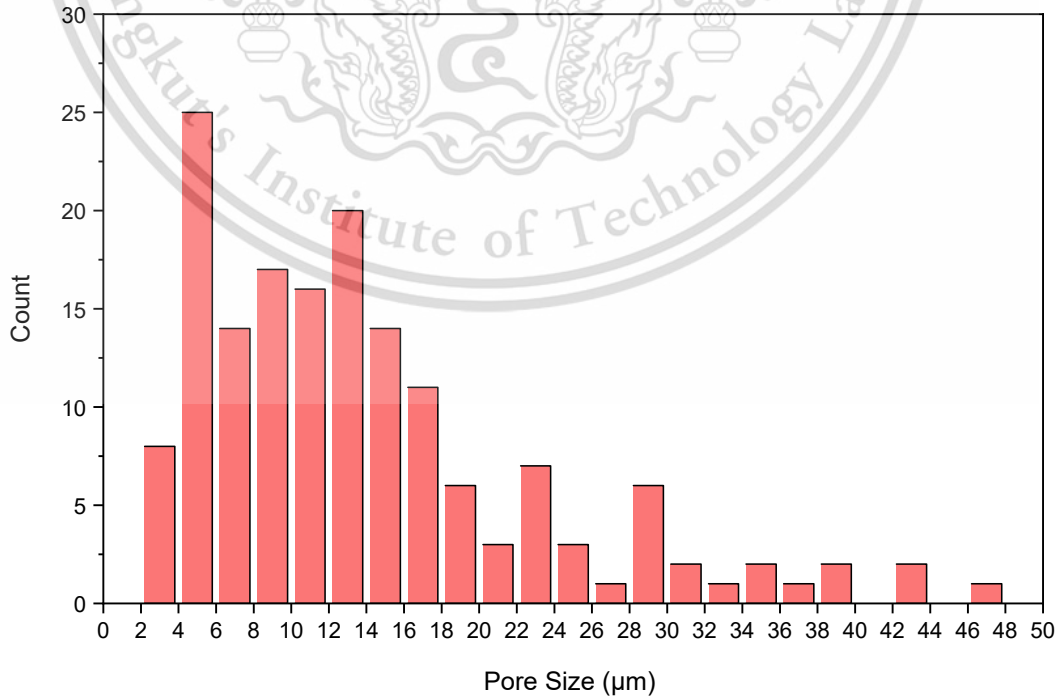

Figure 4.4 Pore size distribution of P-DPF wall surface

4.2 Vehicle Thermal Efficiency and Emissions under Static Conditions

This section mainly focuses on investigating the impact of cordierite P-DPF on exhaust gas temperature (EGT), pressure drop, fuel flow rate, brake thermal efficiency (BTE), and emission characteristics using biodiesel blends B10 and B100. The experiment was conducted at various engine speed and load conditions, with and without the introduction of cordierite partial-flow diesel particulate filter (P-DPF).

4.2.1 Exhaust Temperature and Pressure Drop

Exhaust gas temperature (EGT) under all tested conditions measured by thermocouple is shown in **Figure 4.5**. The results show that an increase in engine load causes a corresponding rise in EGT, attributed to the greater amount of fuel required to produce the necessary power. Furthermore, it increases with engine speed due to a shorter interval for heat to transfer through the cylinder wall. Canakci et al. [64], Muralidharan and Vasudevan [65] reported a drop in EGT with biodiesel ratio while Pramanik [66] and Ramadhas et al. [67] presented the reverse, where the addition of biodiesel causes EGT to increase. This study observes that higher biodiesel content causes a reduction in EGT, which can be attributed to fuel properties. The atomization process is greatly influenced by fuel density, viscosity, distillation temperature, and heat of vaporization [68]. High-density fuel with increased biodiesel content requires more energy to atomize and vaporize fuel into vapor, with the heat coming from the surrounding hot medium inside the combustion chamber. This results in a lower combustion temperature and, subsequently, exhaust gas temperature. The introduction of P-DPF results in an elevation of EGT that can be explained by the reduced exhaust flow and an elevated power demand needed to overcome additional pumping work. Furthermore, EGT increases due to the elevated kinetic energy of residual exhaust molecules resulting from backpressure between the P-DPF and engine. Based on the findings, EGT varies between 322°C and 495°C when utilizing B10, and between 306°C and 463°C when employing B100. When the P-DPF is introduced, EGT extends from 335°C to 499°C with B10 and from 315°C to 469°C with B100.

Figure 4.6 illustrates the observed pressure drops under various engine conditions, both with and without the introduction of P-DPF. The pressure drop is defined as the pressure difference before and after P-DPF. In the cases where only fuel is used, the pressure drops appear to be zero since P-DPF is not installed. When P-DPF

is installed, it is evident that the pressure drop increases with increasing engine speed and load, attributed to the greater exhaust flow rate. The minimum and maximum levels recorded are 1.4 kPa and 7.1 kPa, respectively, while there is minimal difference between different biodiesel blends. The introduction of P-DPF increases pressure drop due to elevated exhaust flow resistance. This can impact fuel flow rate, thermal efficiency, and emissions, which will be discussed in the following section.

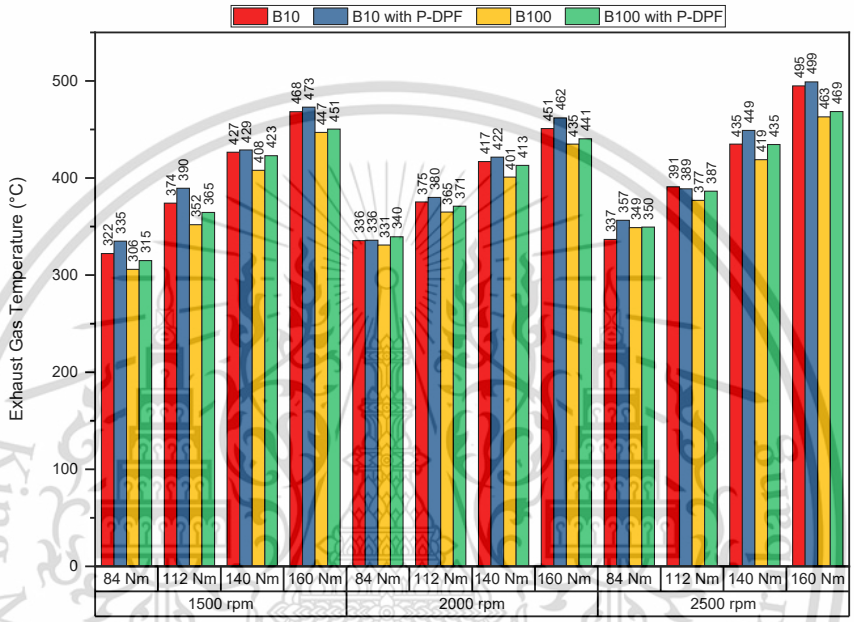

Figure 4.5 Exhaust gas temperatures at various engine conditions

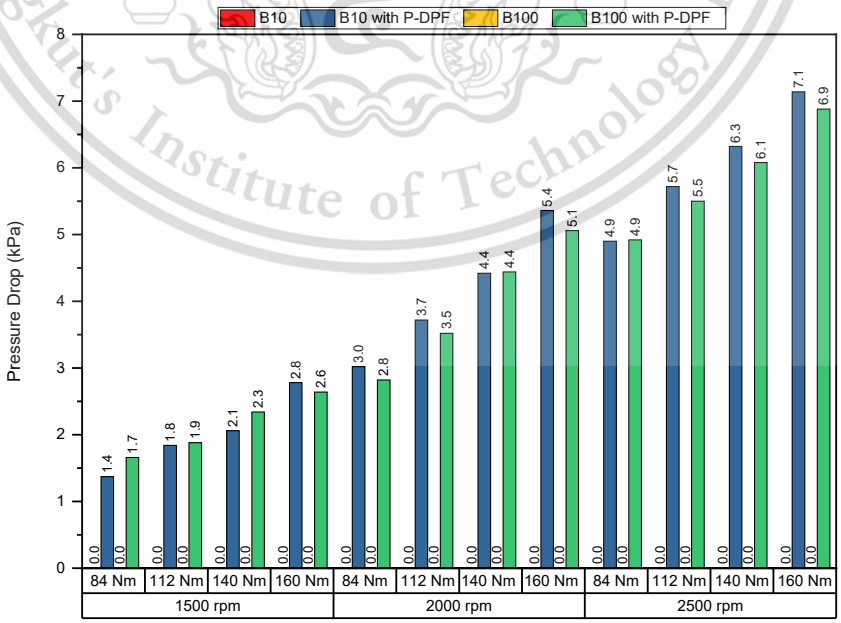

Figure 4.6 Pressure drops with and without P-DPF under various conditions

4.2.2 Vehicle Thermal Efficiency

Vehicle performance, including fuel flow rate, brake-specific fuel consumption (BSFC), brake-specific energy consumption (BSEC), and brake thermal efficiency (BTE), is investigated in comparison with and without the introduction of cordierite partial-flow diesel particulate filter (P-DPF) utilizing biodiesel blends B10 and B100. In **Figure 4.7**, fuel flow rates at different engine conditions, measured in grams per second (g/s), are shown. It is evident that an increase in engine speed and load results in increased fuel flow rate due to the demand for a greater amount of fuel at higher output power. In comparison between fuels, B100 indicates a higher rate of fuel consumed at all tested conditions due to its lower heating value [69]. On average, the excess level is recorded at 11%. The installation of P-DPF causes an elevated fuel flow rate due to the escalation of backpressure. However, the disparity is negligible because of the partial filtration mechanism of the cordierite P-DPF, with 1.6% and 0.5% utilizing B10 and B100, respectively.

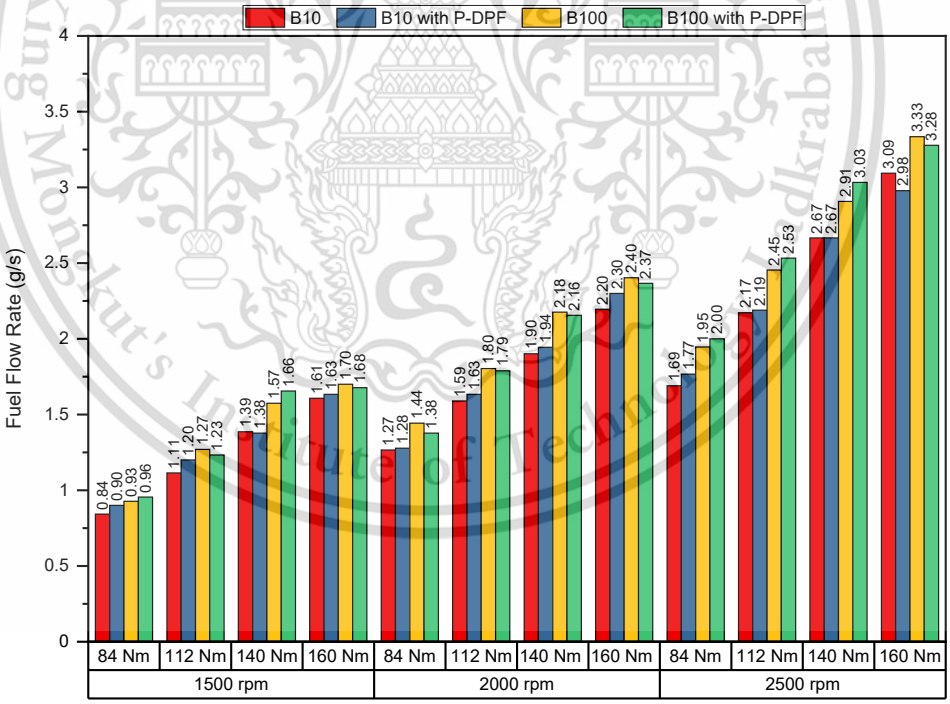

Figure 4.7 Fuel flow rate at various engine conditions

BSFC refers to the amount of fuel consumed that corresponds to a unit of output power. It can be used to compare how efficiently the fuel is converted to useful work at different power outputs. **Figure 4.8** illustrates the levels of BSFC

calculated from fuel flow rate and power output, shown in grams per kilowatt-hour (g/kWh). Increased load at constant engine speed reduces BSFC, indicating enhanced fuel conversion efficiency. More fuel is injected at higher loads to generate higher power, causing elevated combustion temperatures. The higher temperature within the combustion chamber promotes better atomization and vaporization of the fuel, leading to improved mixing with air. This, in turn, enhances combustion efficiency. Furthermore, a higher temperature on the inside surface of the cylinder wall reduces the amount of heat transferred to the cooling water since the temperature difference between the cylinder wall surface and the in-cylinder area is minimized. Utilizing biodiesel B100 leads to an 11.7% increase in BSFC compared to B10 due to its lower heating value. This increment shows that a higher biodiesel ratio results in elevated BSFC, a phenomenon similarly observed by Can [33]. Specifically, the average BSFC under all tested conditions for B10 and B100 is recorded at 247 g/kWh and 275 g/kWh, respectively. It is observed that there is not much difference in BSFC when P-DPF is installed, with values of 252 g/kWh when utilizing B10 and 276 g/kWh when utilizing B100, representing increases of 2.2% and 0.4%, respectively.

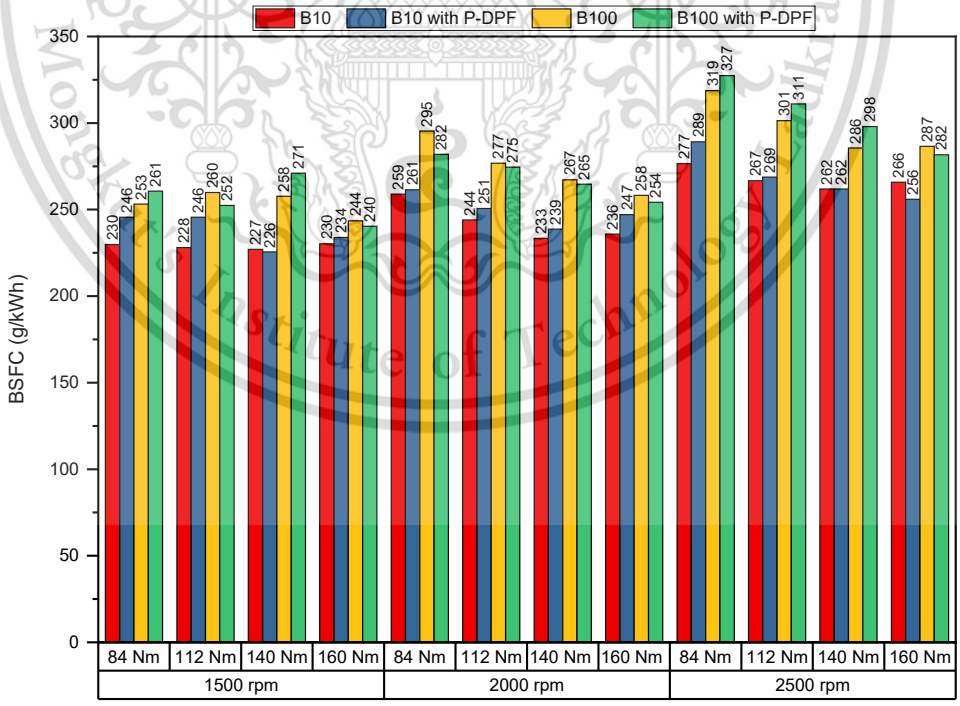

Figure 4.8 Brake-specific fuel consumption at various engine conditions

Brake-specific energy consumption (kJ/kWh) indicates the efficiency of obtaining energy from fuel to produce a unit of output power, allowing for an appropriate comparison of fuels with different heating values. **Figure 4.9** illustrates a variation in BSEC at various engine speeds, ranging from low to medium engine loads. At a constant engine speed, BSEC exhibits a decreased trend when increasing load because of less heat loss at a higher load. Despite having a higher BSFC, biodiesel B100 leads to a 3% decrease in BSEC compared to commercial B10. The presence of available oxygen atoms in fuel molecules and a higher cetane number, which enhance combustion efficiency, are potential reasons for this reduction despite the lower heating value, high viscosity, and higher boiling point of biodiesel B100. The introduction of P-DPF causes an increase in BSEC at a level identical to that of BSFC, with 2.2% and 0.4% using B10 and B100, respectively.

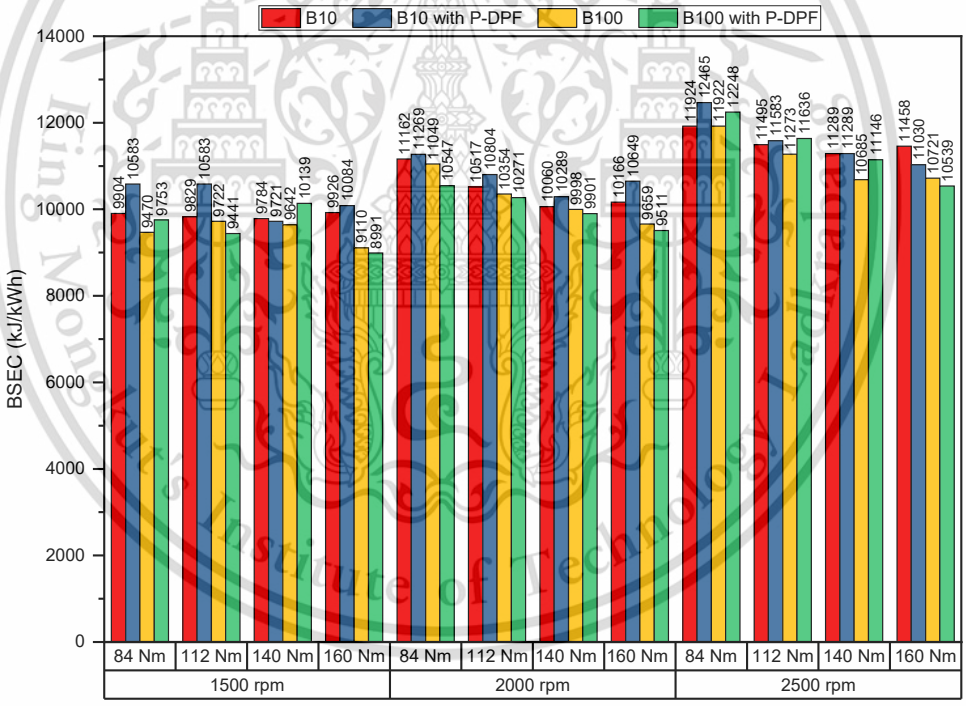

Figure 4.9 Brake-specific energy consumption at various engine conditions

In **Figure 4.10**, the energy consumption rate, or input energy, signifies the necessary energy required to produce a unit of power, typically expressed in kJ/s or kW. Input energy in most of the tested conditions of biodiesel B100 is slightly less than that of B10 due to the trade-off between higher fuel flow rate and lower heating value, with a 3.5% less for B100. This explains the higher brake thermal efficiency of biodiesel

B100 compared to B10 at the same output power, as shown in **Figure 4.11**. In comparison between fuels, the presence of available oxygen in fuel molecules of B100 plays a vital role in facilitating the combustion process, enhancing combustion efficiency, and increasing brake thermal efficiency. Furthermore, its higher cetane number results in a shorter ignition delay, providing a longer interval for fuel/air mixing and combustion duration [70]. As a result, the engine may operate more efficiently with fuel having a higher cetane number, leading to increased BTE. Moreover, high viscosity may also reduce friction loss, which can be a potential parameter for the predominance of B100 compared to B10 in BTE. On average, BTE of B100 is recorded at 35.2%, which is approximately 1.2% higher than that of B10, which is at 34%. The introduction of cordierite P-DPF results in a slight reduction in BTE, at 35.1% and 33.3% for B100 and B10, respectively. It is suggested that the impact of cordierite P-DPF on BTE is minimal due to very low backpressure, with the corresponding variation in BTE being 0.1% and 0.7% for B100 and B10.

In summary, it can be inferred that the introduction of cordierite P-DPF has minimal impacts on fuel flow rate, BSFC, BSEC, and BTE, attributed to its low backpressure due to the partial-flow mechanism.

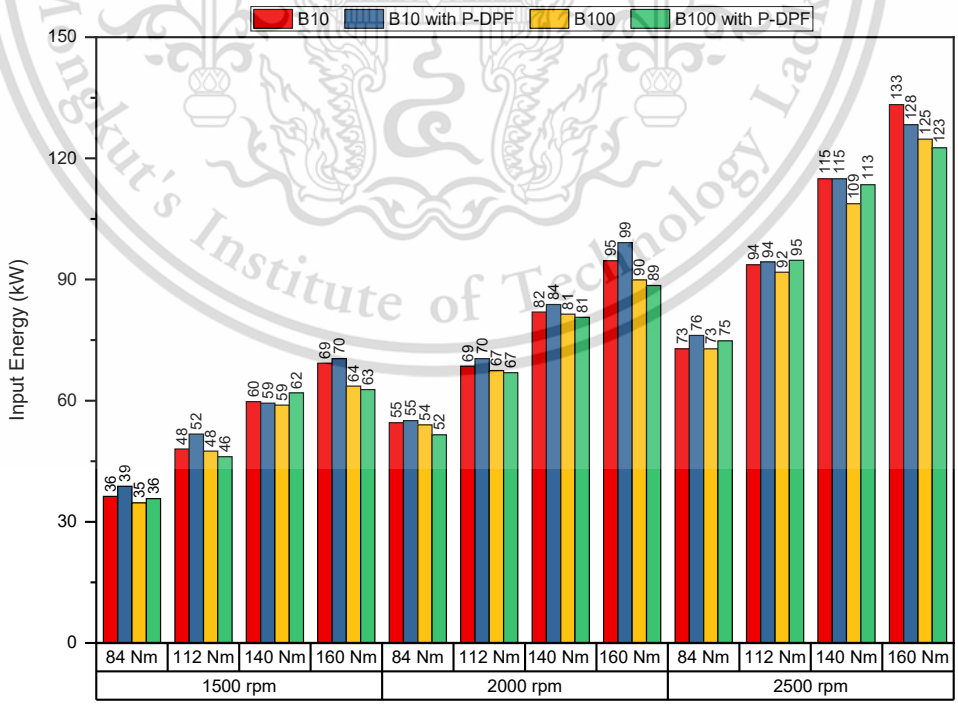

Figure 4.10 Input energy at various engine conditions

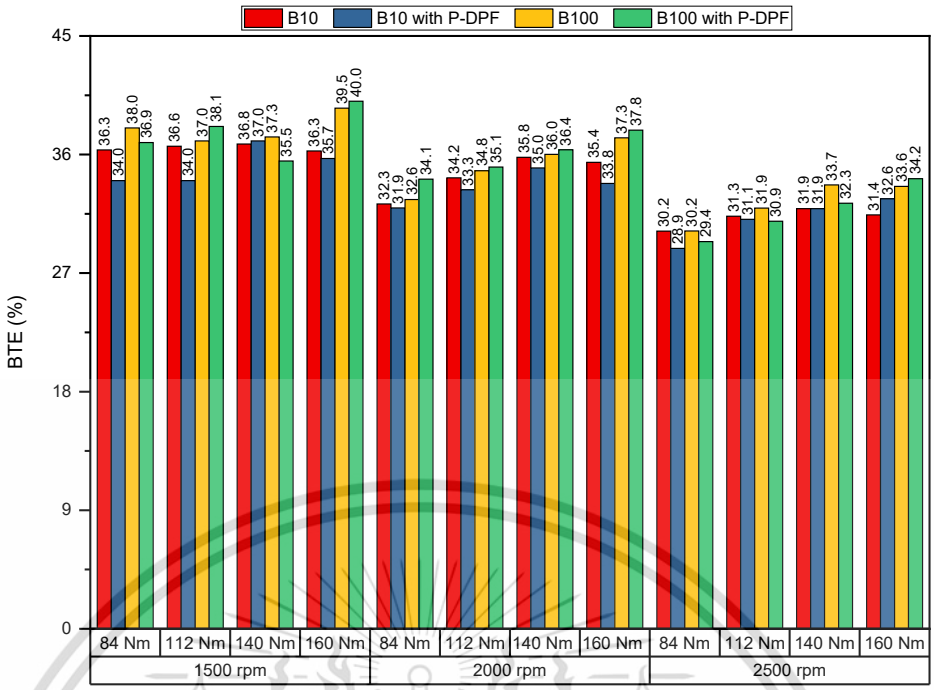

Figure 4.11 Brake thermal efficiency at various engine conditions

4.2.3 Emissions under Static Conditions

The impact of cordierite P-DPF on emission characteristics of the test vehicle is investigated by measuring various exhaust parameters, including equivalent ratio (ϕ), nitric oxide (NO) levels in parts per million (ppm), smoke intensity, carbon dioxide (CO_2), and oxygen (O_2) percentages. The equivalent ratios obtained from the exhaust of the test diesel vehicle under different engine conditions are shown in **Figure 4.12**. It is observed that the equivalent ratio gradually increases with increasing load at a constant engine speed. This trend is attributed to the higher fuel injection rates at heavier loads, while the airflow rate remains steady. On the other hand, the equivalent ratio decreases with engine speed, owing to the elevated turbocharger boost pressure at higher engine speeds, leading to greater air compression in the engine. The increase of biodiesel in the blend leads to a decrease in the equivalent ratio. Biodiesel B100, with approximately 11% oxygen content, results in less air consumption than commercial fuel B10, causing a decreased equivalent ratio. The introduction of cordierite P-DPF leads to an elevation in the equivalent ratio due to the need for injecting more fuel to compensate for the increased backpressure resulting from elevated pumping losses. As shown in the graph, the equivalent ratios of the test diesel vehicle range from 0.37 to 0.70 across all assessed conditions, indicating a lean mixture, which is a general characteristic of diesel engine operation.

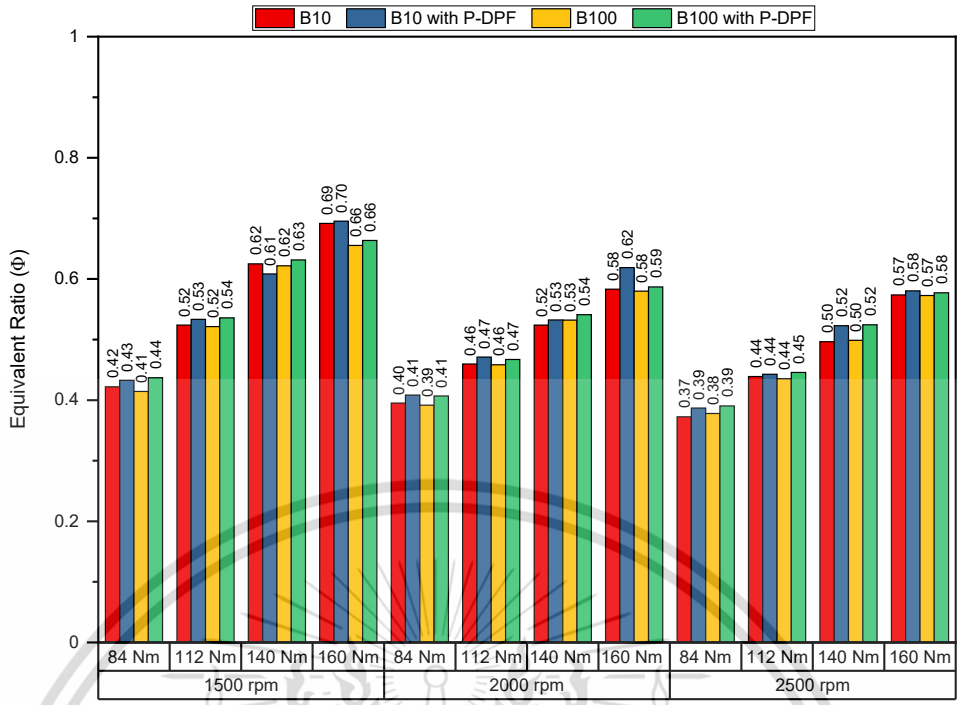

Figure 4.12 Equivalent ratio

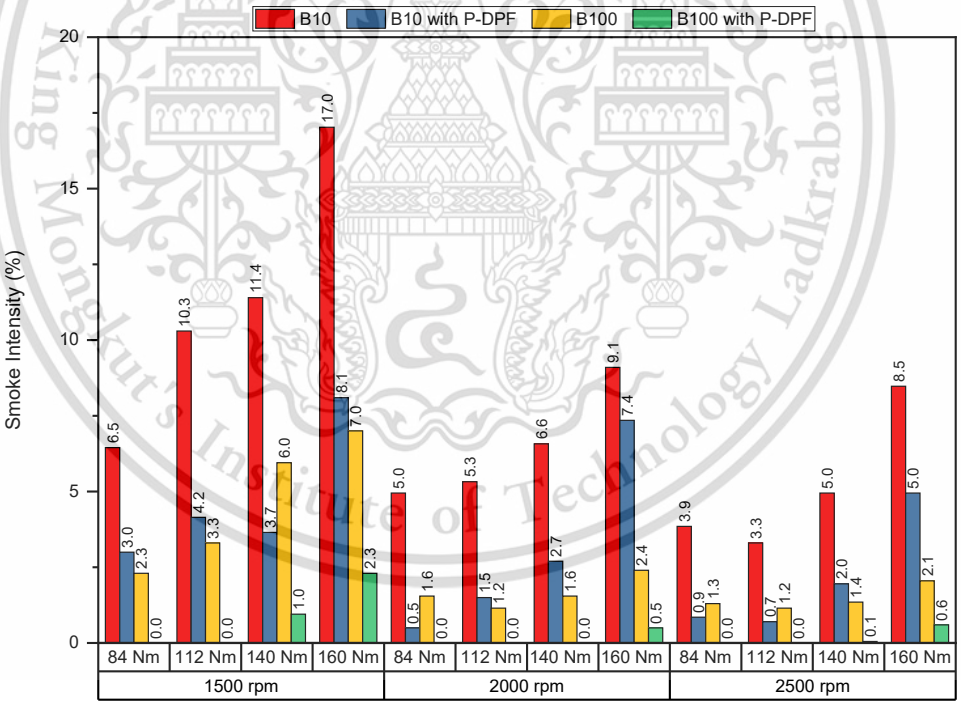

Figure 4.13 Smoke intensity

In **Figure 4.13**, the levels of smoke intensity are illustrated across various engine conditions, comparing scenarios with and without the introduction of P-DPF using biodiesel blends B10 and B100. As the load increases while maintaining a constant engine speed, there is a corresponding rise in smoke intensity. This escalation

correlates with the richer fuel-air mixture required for heavier loads, necessitating more fuel injection to generate increased torque. The results indicate that the highest smoke intensity consistently occurs at 1500 rpm and 160 Nm across all cases. This is because the engine operates inefficiently and generates high PM levels at low speed and high load, reaching 17% when fueled with B10. However, on average, with the integration of P-DPF, there is a notable reduction in smoke intensity, with a decrease of 57% observed when using B10. Remarkably, this reduction becomes more pronounced when employing biodiesel B100, achieving an impressive 86% decrease. This decline is attributed to the filtration mechanism of the partial-flow DPF, which effectively traps particulate matter within its porous walls.

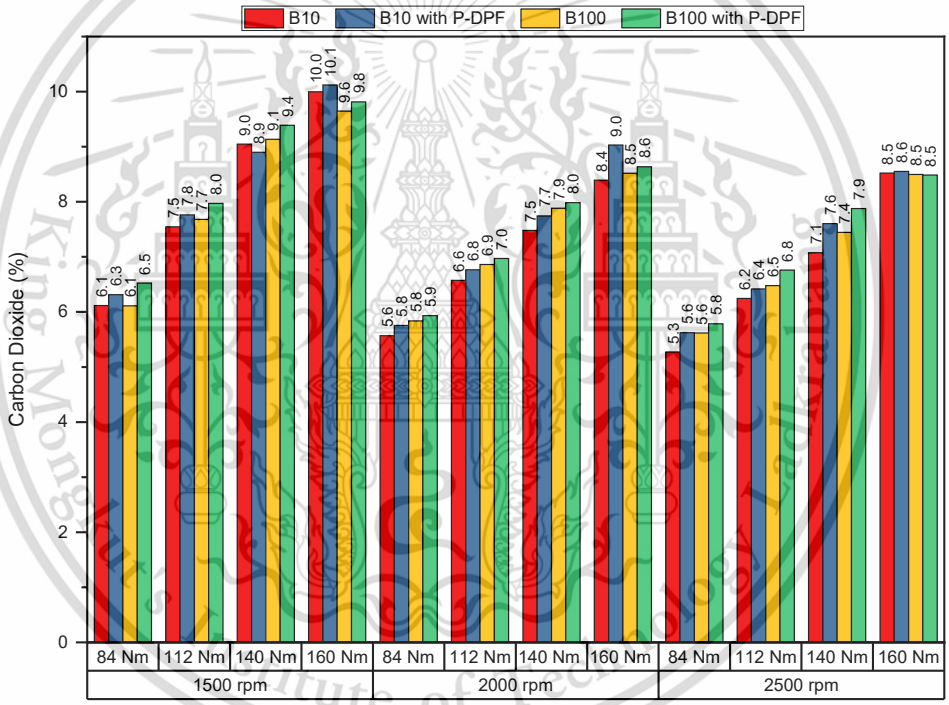

Figure 4.14 Carbon dioxide

Figure 4.14 illustrates the change in carbon dioxide (CO_2) concerning various engine conditions from the test diesel vehicle. The results depict an upward trend in CO_2 with increasing load as the engine speed remains constant. Increased load demands more fuel injection, resulting in elevated CO_2 levels as it is the primary product of combustion. On the other hand, oxygen (O_2) levels exhibit a reverse trend compared to those of CO_2. More fuel injection at heavier loads necessitates more O_2 for combustion, leading to decreased O_2 levels in the exhaust gas. The increased

biodiesel content, with elevated O_2 molecules, results in higher CO_2 from the exhaust due to more complete combustion. Moreover, it also leads to less consumption of O_2 from the air, resulting in higher O_2 levels in the exhaust when using B100 compared to B10, as illustrated in **Figure 4.15**. The introduction of P-DPF as an after-treatment system leads to an increase in CO_2 and decrease in O_2 due to the oxidation of hydrocarbons (HC) and carbon monoxide (CO) into CO_2 with the support of catalyst. Furthermore, trapping and passive soot oxidation via reactions with NO_2 and O_2 inside the P-DPF at appropriate temperatures may also contribute to this phenomenon.

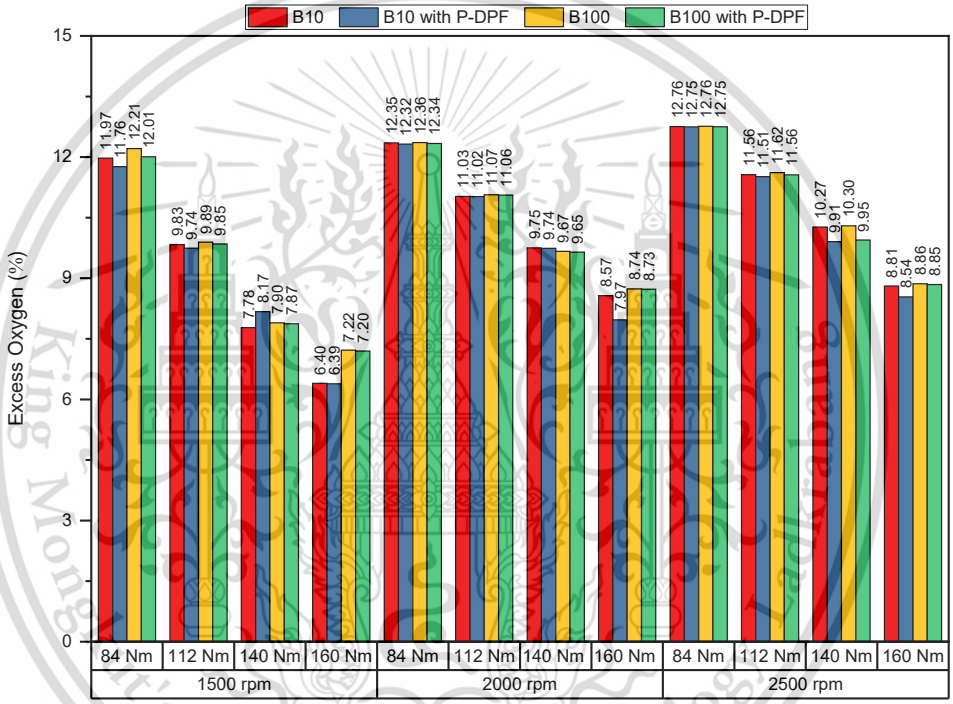

Figure 4.15 Excess oxygen from the exhaust

Nitrogen oxides (NOx) is regarded as one of the toxic gases with a high concentration in the exhaust of diesel engines. It consists of nitric oxide (NO) and nitrogen dioxide (NO_2) with 80-95% and 5-20%, respectively [44]. The amount of NOx is a function of combustion temperature, oxygen concentration, and residence time [4]. **Figure 4.16** indicates the variations in NO emissions with different biodiesel blends and with the introduction of P-DPF. The correlation between NO levels and loads is observed due to elevated in-cylinder temperatures at heavier loads. Biodiesel B100 exhibits lower NO levels compared to B10 in most of the tested conditions due to its lower combustion temperatures. However, some conditions at high engine speed show

a reverse trend, exhibiting a higher NOx amount with B100. This can be explained by the higher cetane number in biodiesel B100, which leads to a shorter ignition delay and, therefore, a longer residence time of the mixture at high temperatures. The introduction of a P-DPF causes an increase in NO emissions due to partial soot oxidation and elevated combustion temperatures from the injection of more fuel, resulting in increases of 3% with B10 and 7% with B100.

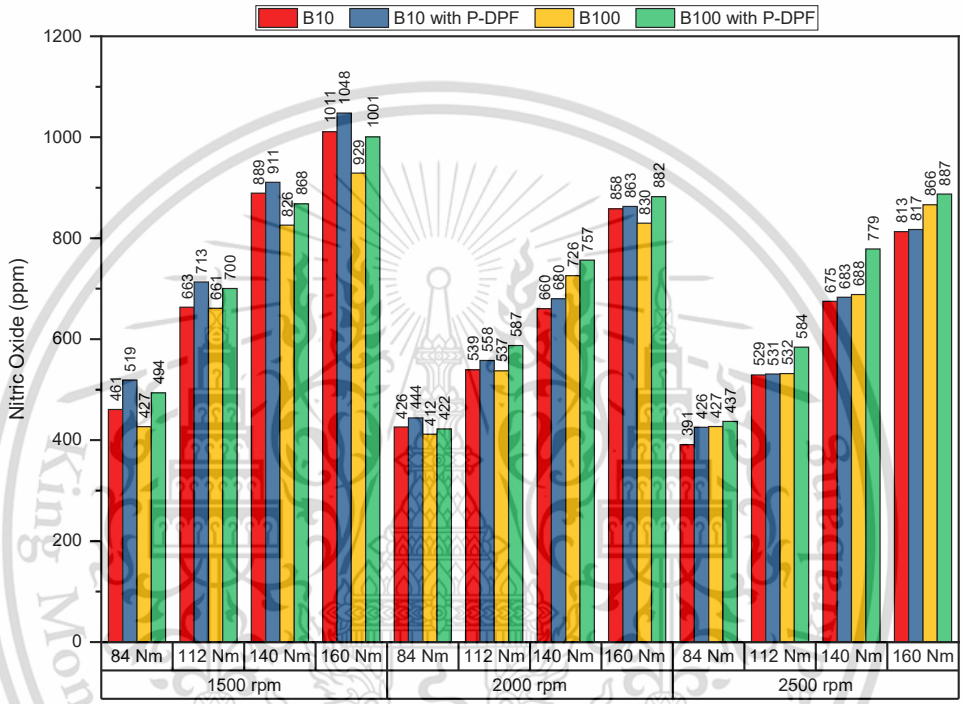

Figure 4.16 Nitric oxide emission from the exhaust

The analysis of smoke intensity, nitric oxide, carbon dioxide, oxygen, and exhaust gas temperature indicates that integrating P-DPF into the system enables simultaneous trapping and oxidizing of soot. Soot is trapped inside porous walls and oxidized to CO_2 by NO_2 and O_2 at appropriate temperatures. The EGTs recorded in all tested conditions range from 315°C to 499°C, which are suitable for forming NO_2 from NO at temperatures above 250°C. Moreover, soot oxidation with O_2 is also possible at temperatures above 350°C [44].

The highest smoke intensity is observed at 1500 rpm and 160 Nm across tested conditions. Paper filters used to trap PM under this condition are examined using scanning electron microscopy (SEM) at magnifications of 2000x and 10,000x to visualize the quantity of trapped PM. **Figure 4.17** shows SEM captures of PMs on paper filters

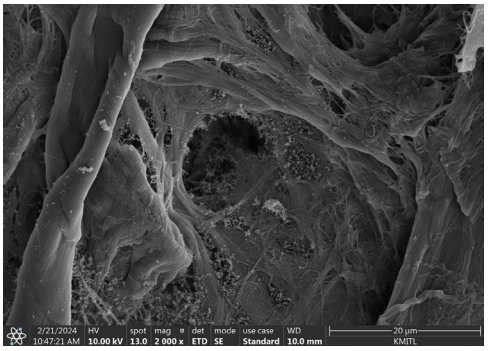

B10

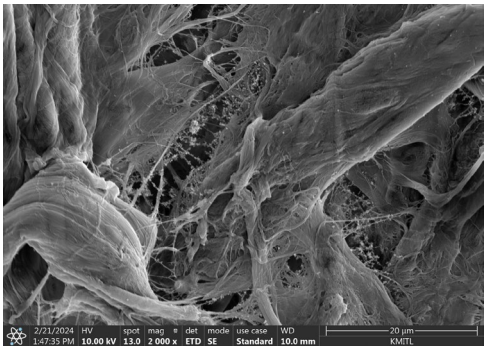

B10 with P-DPF

B100

B100 with P-DPF

(a) 2000x magnification of PMs on paper filters

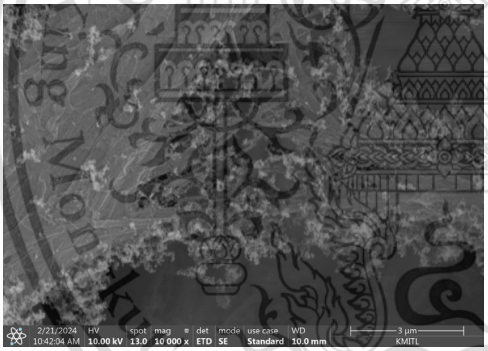

B10

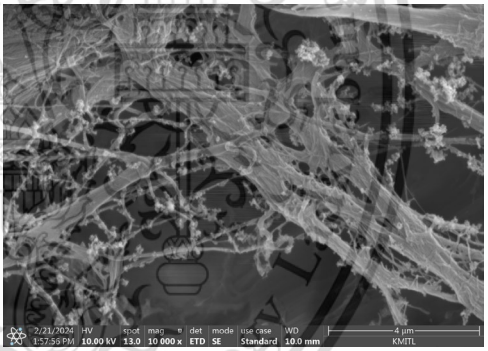

B10 with P-DPF

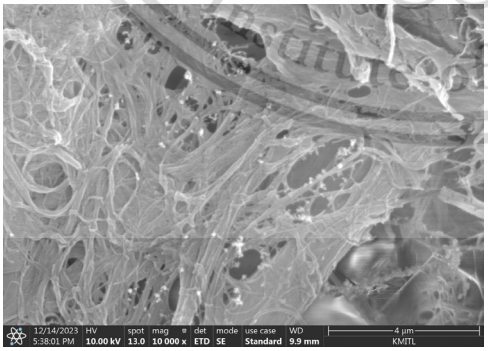

B100

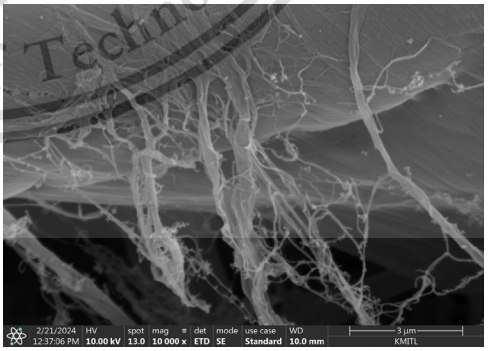

B100 with P-DPF

(b) 10,000x magnification of PMs on paper filters

Figure 4.17 SEM captures of PMs on paper filters at 1500 rpm and 160 Nm with and without P-DPF using biodiesel B10 and B100

under the specified conditions, both with and without the introduction of a P-DPF when utilizing commercial fuel B10 and biodiesel B100. These images illustrate a visible difference and emphasize the significant impact of biodiesel blends and cordierite P-DPF on reducing PMs from the test diesel vehicle. A less dense concentration of PMs is observed on the filter when comparing biodiesel B100 to commercial fuel B10. This is attributed to the higher oxygen content in biodiesel, which leads to better combustion and reduced PM formation compared to B10. Additionally, there is a significant reduction in PM when P-DPF is introduced, with the greatest reduction observed when using biodiesel B100, consistent with the results of smoke intensity.

4.3 Emission Factors of Regulated Pollutants under NEDC

This section examines the impact of a cordierite P-DPF on the regulated emission factors of a light-duty diesel vehicle utilizing commercial fuel B10 and biodiesel B100. The vehicle operates under the new European driving cycle (NEDC) to access emissions including CO, HC, NOx, and PM. Real-time concentrations of gaseous emissions, reported in parts per million (ppm), are measured by gas analyzers, while the concentration of particulate number (PN) is measured by a particle counter, stated in particles per cubic centimeter (#/cm^3). Emission factors (g/km) in each driving cycle, including the urban driving cycle (UDC) and the extra-urban driving cycle (EUDC), are derived from real-time data. The NEDC level is defined as an average of these cycles.

4.3.1 Gaseous Emissions

Figure 4.18 and **Figure 4.19** illustrate the real-time concentrations and emission factors of THC and CO emissions in cases with and without P-DPF utilizing biodiesel B100 and blend B10 when the test vehicle runs under NEDC. A higher concentration is observed in UDC than in EUDC due to differences in the operation characteristics of both cycles. The frequent cold-start operations in UDC with an average vehicle speed of 19 km/h diminish combustion efficiency because the cold engine has trouble combusting the mixture completely, leading to higher concentration in this cycle. On the other hand, a high vehicle speed in EUDC at 63 km/h leads to better combustion due to elevated engine temperature, resulting in a lower concentration. A similar observation was also reported by Grigoratos et al. [71]. Moreover, a remarkable disparity is observed between the acceleration and

deceleration phases, with a rise in THC and CO emissions during acceleration and a drop during deceleration. These phenomena come from the scenarios in which the combustion chamber receives a greater amount of fuel during the acceleration phase to overcome instantaneous load, while fuel injection is reduced due to the activation of the cut-off function in the deceleration period. In a comparison between fuels, it is found that B100 shows a notable reduction in THC while CO is comparable to B10. Specifically in THC, the emission factor when employing B100 is 0.058 g/km compared to 0.099 g/km of B10, showing a 41% reduction. This reduction is attributed to the superior oxygen content that enhances combustion quality. This result aligns with the findings noted by Bakeas et al. [72], indicating decreased HC and CO emissions with the addition of biodiesel. The introduction of P-DPF leads to a corresponding reduction of 22% and 14% THC emission when utilizing B10 and B100, while that of CO emission is 20% and 13%. These reductions are attributed to the support of catalyst in chemical conversions that form CO_2 and water vapor from the reactions of HC and CO with O_2 [4].

Figure 4.20 shows NOx real-time concentration and emission factor when operating under NEDC. The concentration markedly increases in EUDC, which correlates with the high vehicle speed. The larger amount of injected fuel at higher vehicle speed raises combustion temperature, leading to this increase [73]. As a result, the highest concentration in EUDC is approximately 270 ppm compared to 90 ppm in UDC. Based on the observed results, tailpipe NOx emissions are 2% lower with biodiesel B100 compared to B10, measuring 1.15 g/km and 1.18 g/km, respectively. The higher heat of vaporization and lower heating value reduce in-cylinder temperature, consequently reducing NOx [74]. There is a slight reduction when P-DPF is installed downstream of the system, with 1.06 g/km and 1.07 g/km, corresponding to a decrease of 7% and 9% with B100 and B10. This can be attributed to the utilization of NO_2 as an oxidant to oxidize trapped soot into CO_2 at temperatures as low as 250°C [44]. Moreover, backpressure may cause some portion of the exhaust gas to remain in the combustion chamber until the following combustion cycle, thus diluting the new air-fuel mixture and reducing the oxygen concentration in the combustion chamber. This, in turn, lowers the peak temperature and pressure of the combustion process, consequently

reducing NOx emission, which is a byproduct of high-temperature and high-pressure combustion.

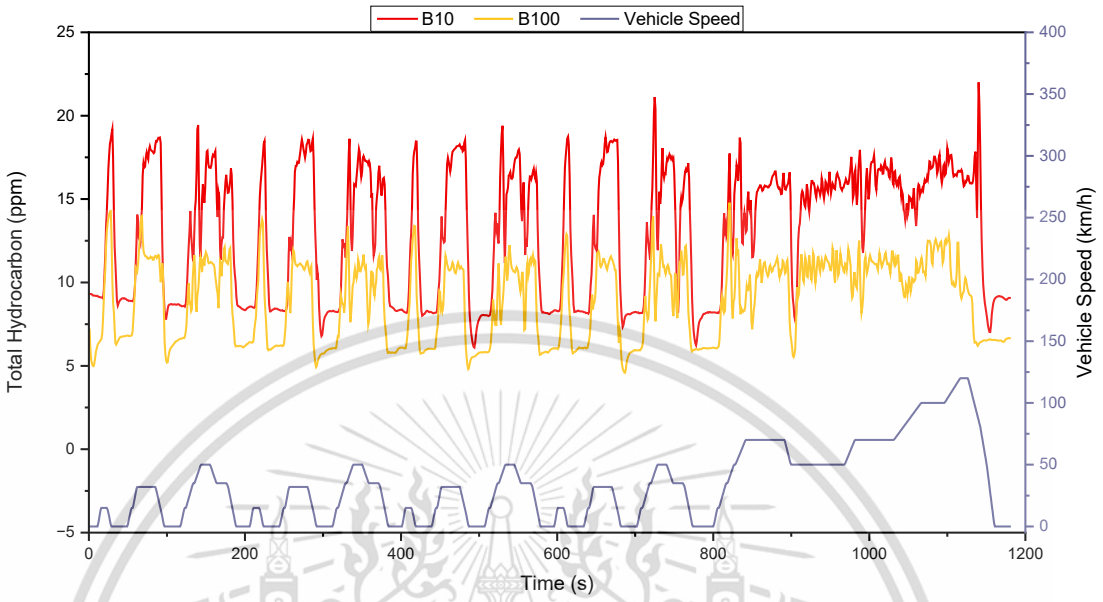

(a) real-time concentration of total HC

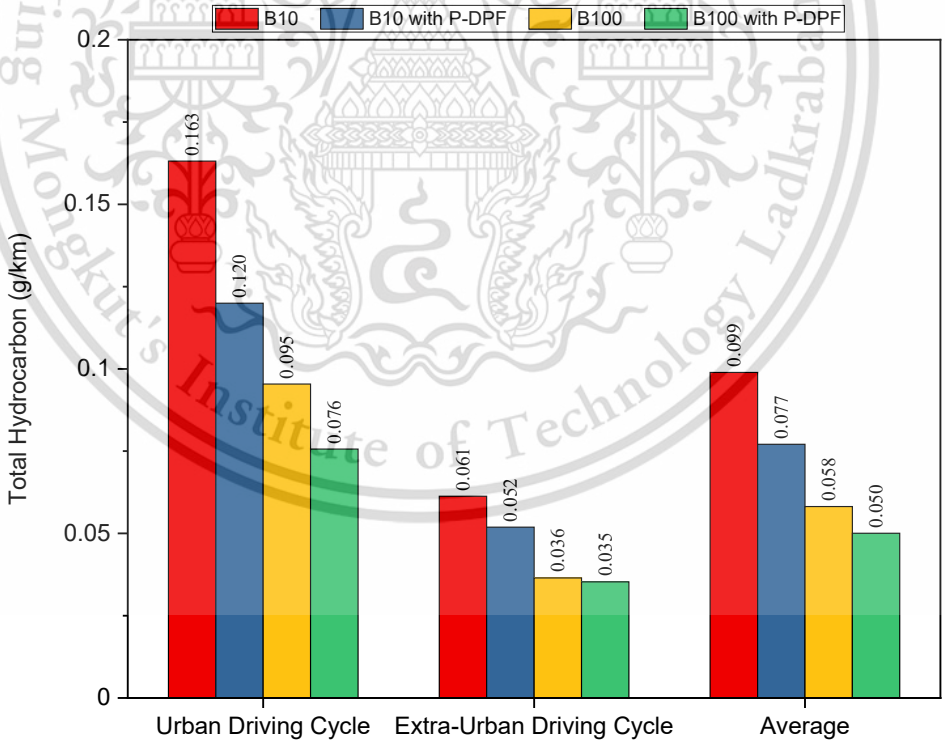

(b) THC emission factor

Figure 4.18 THC emission with and without P-DPF under NEDC

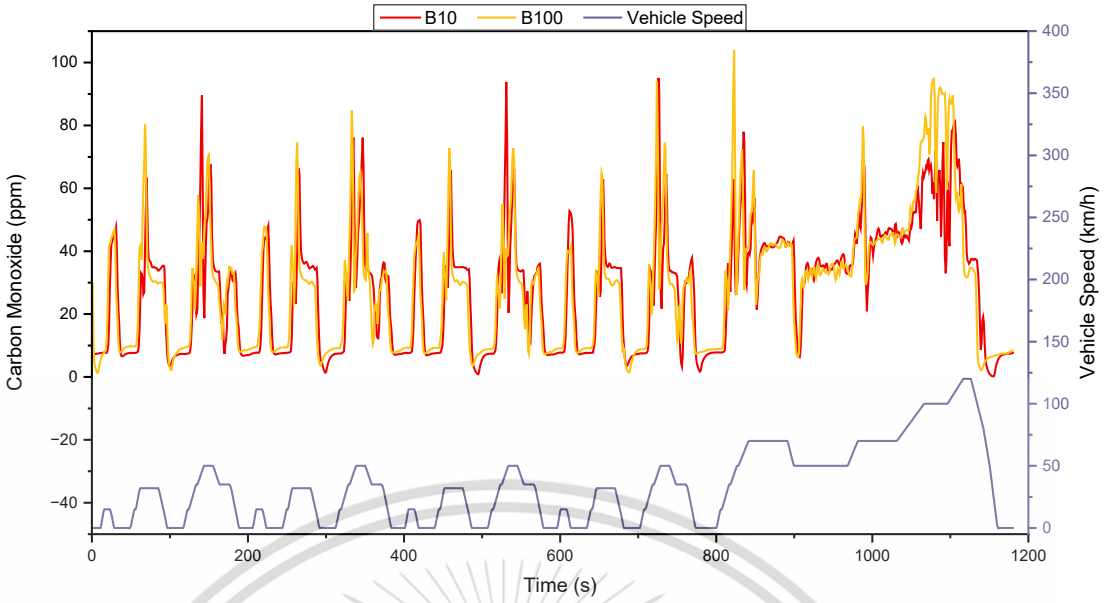

(a) real-time concentration of CO

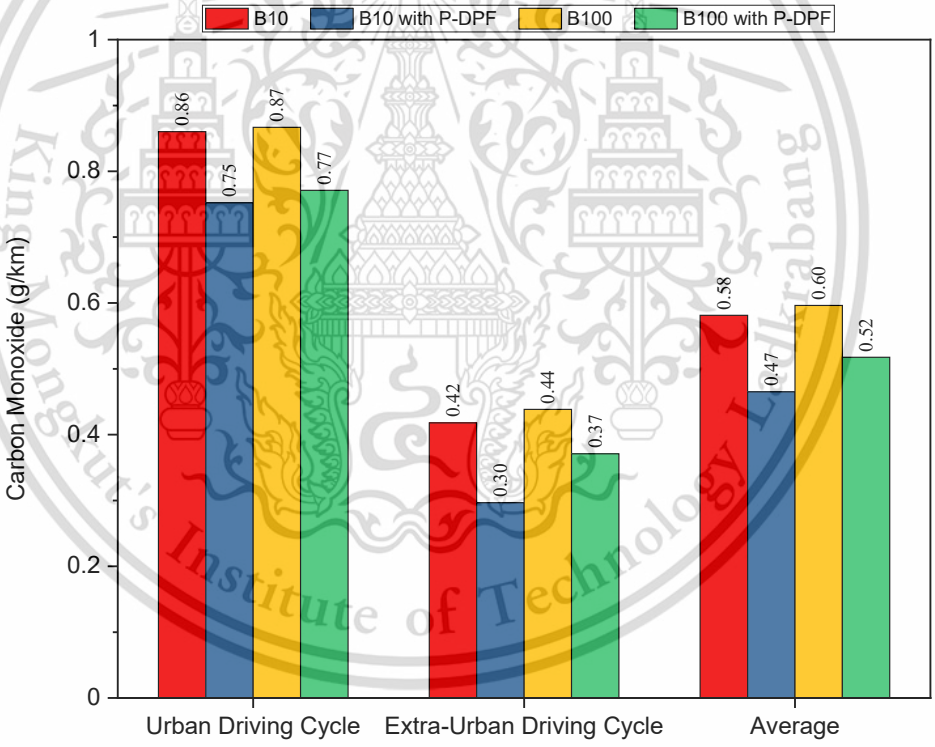

(b) CO emission factor

Figure 4.19 CO emission with and without P-DPF under NEDC

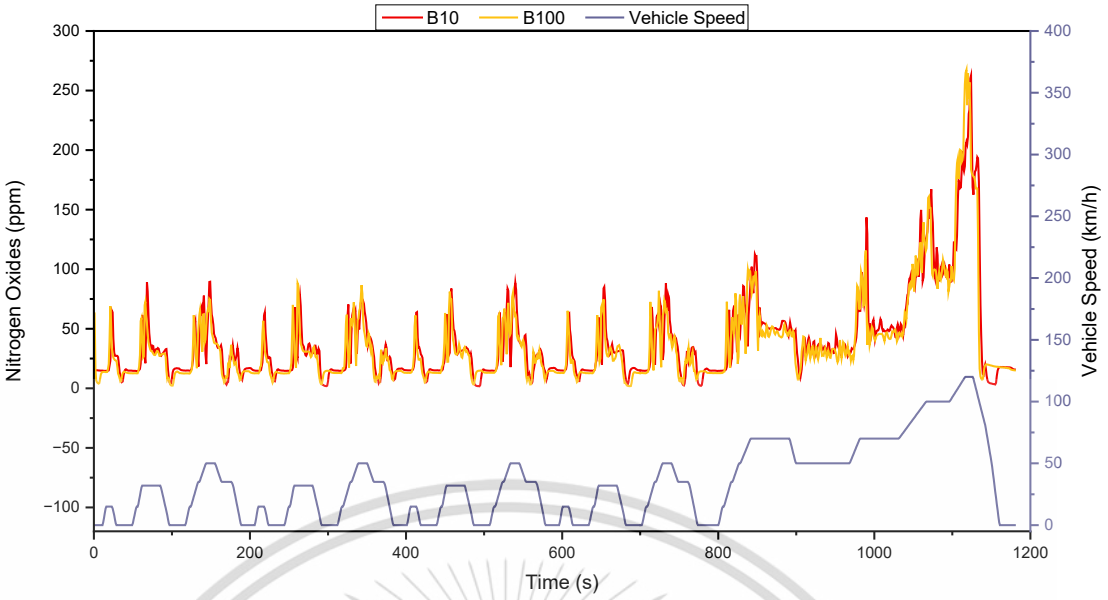

(a) real-time concentration of NOx

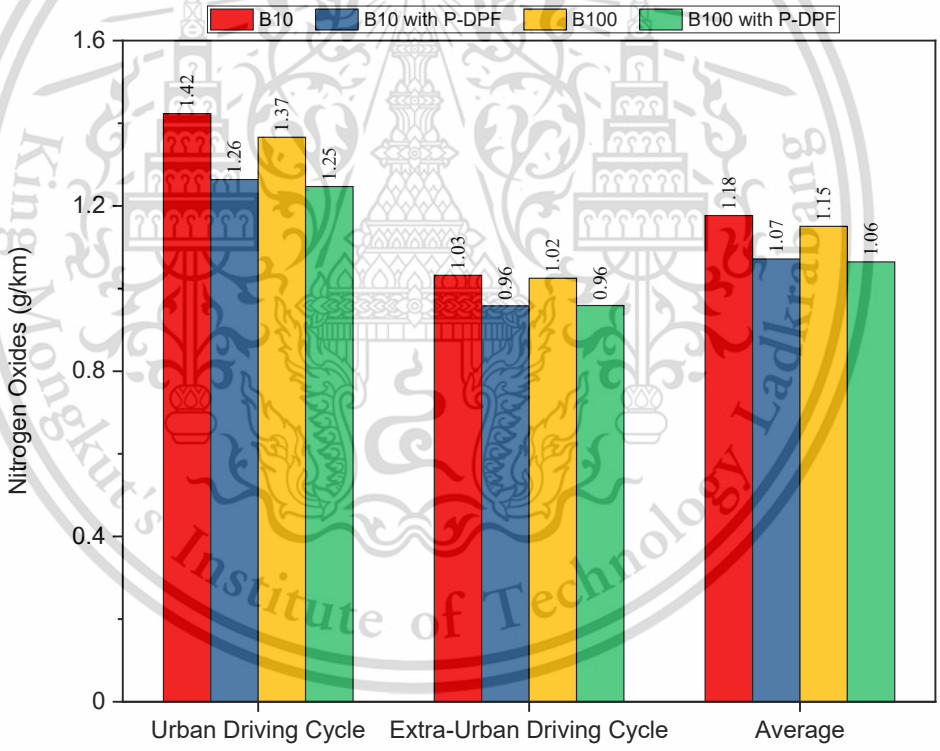

(b) NOx emission factor

Figure 4.20 NOx emission with and without P-DPF under NEDC

4.3.2 Particulate Matter

The detailed results of particulate matters, including the real-time concentration and PN factor in cases with and without P-DPF utilizing commercial fuel B10 and biodiesel B100 under NEDC, are shown in **Figure 4.21**. The concentration of PN is significantly affected by the cold-start operation characteristics in UDC. The tailpipe PN peak concentration when employed with B10 shows a higher value, measuring 8.08×10^{6} #/cm^3. The corresponding result when fueled with B100 is $4.04\text{x}10^{6}$ #/cm^3. The higher concentration in UDC is attributed to the lower cylinder temperature resulting from frequent start-stop events. At this point, low temperature causes improper fuel-air mixing and leads to poor fuel atomization and vaporization, causing incomplete combustion. However, the concentration decreases as it operates in EUDC with an average vehicle speed of 63 km/h. The corresponding peak concentration for B100 and B10 in this cycle is 3.66 $\text{x}10^{6}$ #/cm^3 and 6.86 $\text{x}10^{6}$ #/cm^3. This reduction is attributed to the high in-cylinder temperature at high vehicle speeds, with fewer heat losses through the cylinder wall due to a low-temperature difference between the cylinder wall and in-cylinder temperature. The introduction of P-DPF leads to a remarkable decrease in PN peak concentration. It exhibits 32% and 53% when fueled with B10 and B100, respectively.

As shown in **Figure 4.21(b),** the tailpipe PN factor when fueled with B100 is 45% less than that of B10, with $6.20\text{x}10^{13}$ #/km compared to $1.12\text{x}10^{14}$ #/km. Despite the elevated amount of injected fuel due to its lower heating value, vehicle fueled with biodiesel emits lower PN than B10. The complete fuel oxidation contributed by the availability of 11% oxygen content even in locally rich zones is a practical explanation for the reduction [75]. The combination of P-DPF with fuels B10 and B100 results in significant PN reduction, recorded at $7.18\text{x}10^{13}$ #/km and $3.93\text{x}10^{13}$ #/km, representing a 36% and 39% decrease, respectively. Furthermore, more than 59% of PM mass is reduced by P-DPF for both fuels, with a slight advantage for biodiesel B100 at 60%, as shown in **Figure 4.22**. Specifically, the mass of PM under NEDC when fueled with B10 and B100 is 0.032 g/km and 0.022 g/km, while P-DPF further reduces it to 0.013 g/km and 0.009 g/km, respectively. The higher oxygen content within biodiesel is an excellent parameter that reduces 32% PM mass compared to commercial B10. Besides, alternately clogged channels at the outlet of P-DPF force a partial exhaust to

flow through while trapping PM inside the porous walls. Moreover, simultaneously trapping and partial soot oxidation may occur by utilizing NO_2 and O_2 as oxidants to convert soot to CO_2 at temperatures above 250°C and 350°C, respectively.

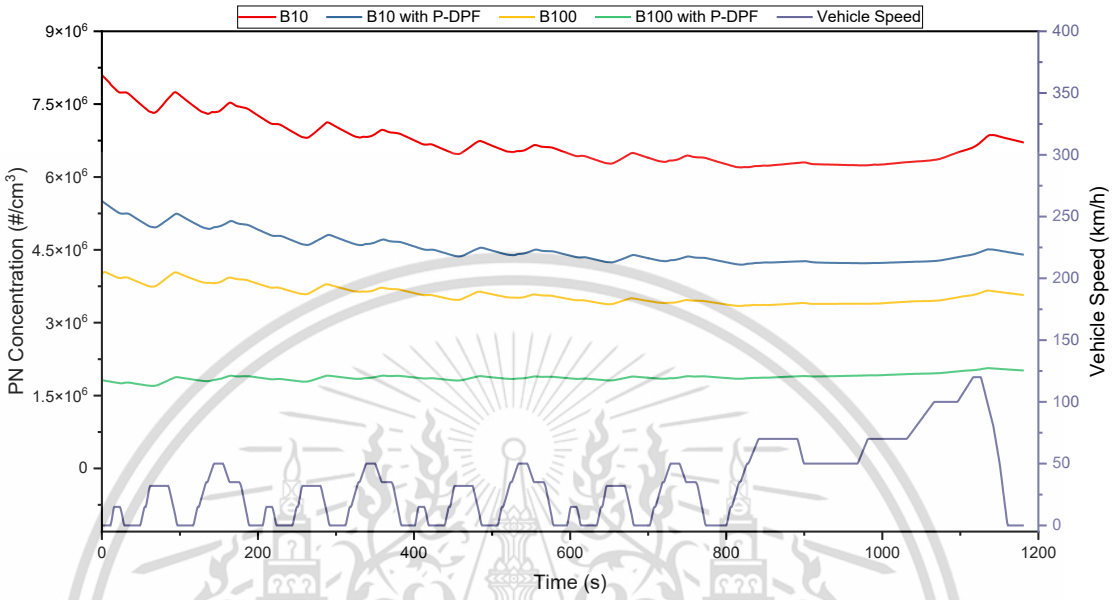

(a) real-time concentration of PN under NEDC

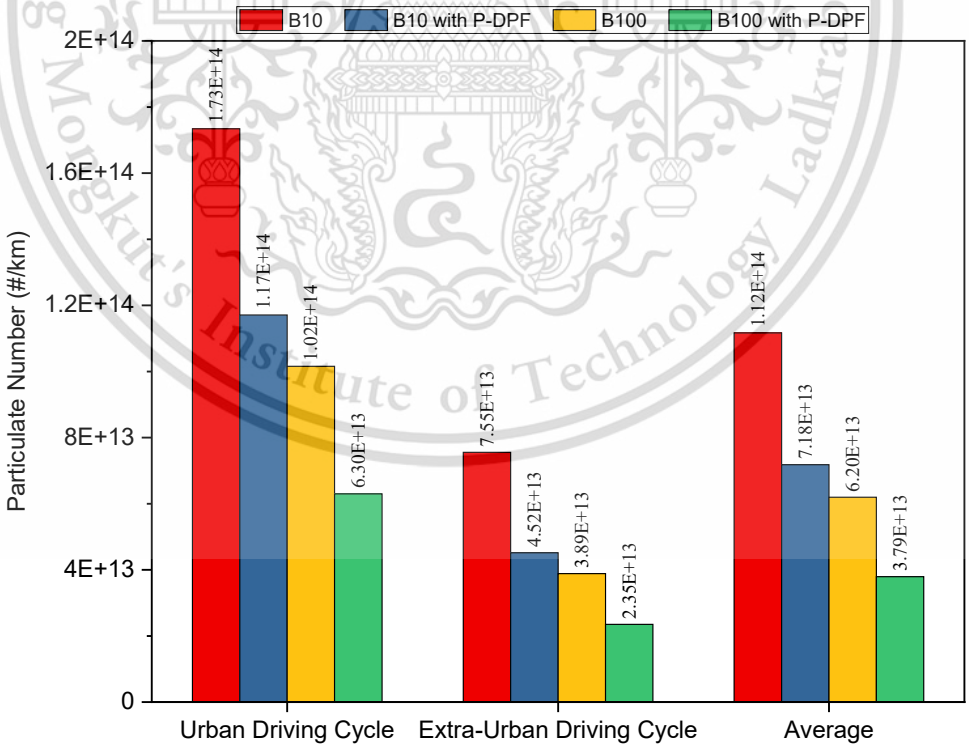

(b) PN factor

Figure 4.21 PN with and without P-DPF under NEDC

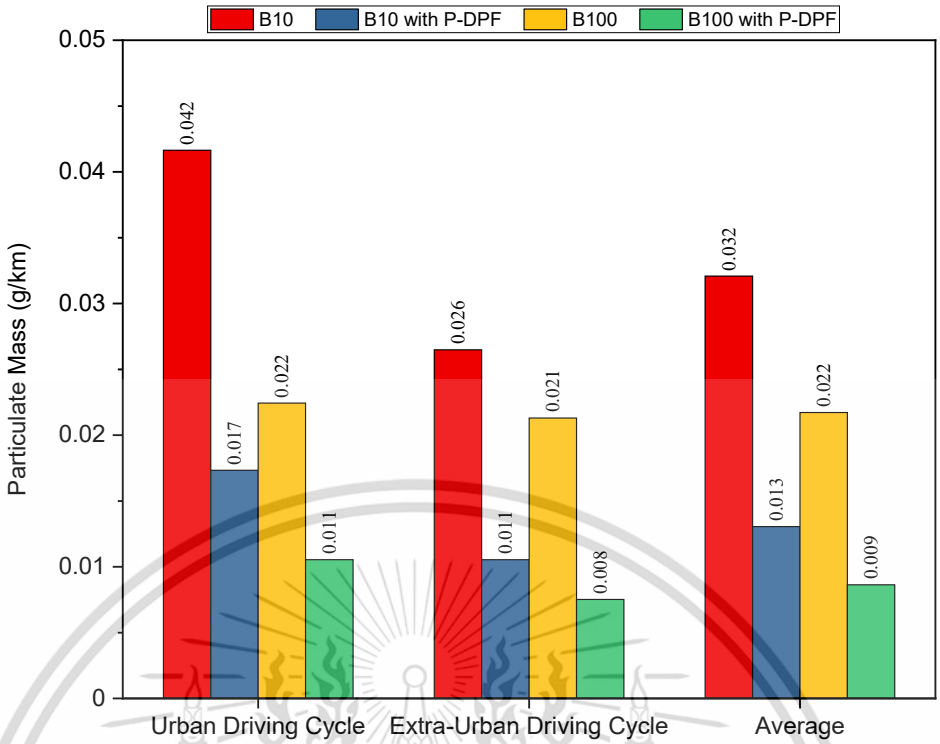

Figure 4.22 PM mass factor with and without P-DPF under NEDC

In a hypothetical comparison, the concentration of PM in Bangkok in 2023 is 28.4 micrograms per cubic meter (μg/m^3) [76], while the contribution of diesel vehicles is 43.7% [77]. Supposing that B10 is the commercial fuel mainly used for diesel vehicles in Bangkok. The installation of cordierite P-DPF reduces PM concentration in the air to 11.6 μg/m^3, which is a 59% reduction. Additionally, when all vehicles are fueled with B100 and equipped with P-DPF, a 73% reduction in PM concentration can be achieved compared to vehicles fueled with B10 without P-DPF, resulting in a concentration of 0.009 μg/m^3.

The use of untreated diesel vehicles in developing countries raises significant concerns about their effects on human health and the environment. Biodiesel has emerged as an effective solution to these issues. However, increasingly stringent emission regulations may necessitate an even more effective solution. A partial-flow P-DPF can be a practical solution when combined with biodiesel to reduce harmful emissions from diesel vehicles. This approach demonstrates its effectiveness in reducing toxic emissions in older diesel vehicles that lack an after-treatment system with minimal modifications.

CHAPTER 5
CONCLUSION

This study investigates the impacts of a ceramic-based partial-flow diesel particulate filter (P-DPF) on fuel consumption, brake thermal efficiency, and emission characteristics of a light-duty diesel vehicle utilizing commercial fuel B10 and biodiesel B100. To better understand the material characteristics of the filter's substrate, the microscale parameters of the filter have been inspected using scanning electron microscopy (SEM), energy dispersive X-ray spectroscopy (EDS), and ImageJ software. Subsequently, two distinct setups are conducted on the chassis dynamometer under steady-state conditions and under the new European driving cycle (NEDC) to compare the results with and without the introduction of P-DPF. In the initial test, the fuel flow rate is measured at various engine speeds and loads, while the exhaust gas temperature and pressure drop are collected by thermocouple and pressure sensor at positions before and after P-DPF. Furthermore, exhaust parameters are also explored in this section. The effectiveness of P-DPF in reducing regulated emissions is evaluated under the NEDC in the second test. The concentration and emission factor of pollutants are discussed.

The material analysis indicates that the filter's wall thickness varies from 210 to 212 μm. The channel width is observed to be between 1200 to 1240 μm, while the coating thickness ranges from 38 to 129 μm. On average, the corresponding dimensions of wall thickness, channel width, and coating thickness are 211, 1220, and 63 μm. The Archimedes method is applied to define the porosity of the filter, finding that the filter's porosity is approximately 66%. Moreover, SEM images of the filter's substrate and ImageJ software are used to determine the pore fraction and size. It indicates that pores occupy around 58%, with the mean pore size being 14 μm. The elemental composition analysis by SEM-EDS reveals that the substrate of P-DPF is mainly made of oxygen, magnesium, aluminum, and silicon. It is found that the substrate of P-DPF is made of cordierite, while the catalyst material is a ceria-zirconia oxide.

The outcomes of the steady-state condition test on the chassis dynamometer show that installing P-DPF causes elevated backpressure due to increased exhaust flow

resistance, with recorded levels from 1.4 kPa to 7.1 kPa under tested conditions. Meanwhile, the installation leads to an increase in exhaust gas temperature because the injection of more fuel is required to compensate for additional pumping losses due to backpressure. Using B100 increases the fuel flow rate by 11% compared to B10 because of its lower heating value. However, it results in a 3% decrease in BSEC and a 1% increase in BTE compared to B10. The available oxygen atoms in the fuel molecules and the higher cetane number improve combustion efficiency. When P-DPF is installed downstream of the exhaust system fueled with commercial B10 and biodiesel B100, the fuel flow rate exhibits a corresponding increase of 1.6% and 0.5%, which originates from elevated backpressure. Meanwhile, the respective disparity in terms of brake-specific fuel consumption in cases with and without P-DPF is 2.2% and 0.4%. It is suggested that the impact of cordierite P-DPF on BTE is minimal due to low backpressure, with the corresponding variation being 0.1% and 0.7% for B100 and B10. It can be inferred that the introduction of cordierite P-DPF has a negligible impact on fuel consumption and BTE, attributed to its low backpressure. In terms of emissions, smoke intensity is significantly reduced by biodiesel and P-DPF, averaging from 57% to 86%. This reduction can be visually observed in SEM images taken from the paper filters. The introduction of P-DPF leads to increased CO_2 and decreased O_2 due to the oxidation of HC and CO into CO_2 with the support of the catalyst. Moreover, simultaneous soot trapping and passive oxidation inside the P-DPF may contribute to this phenomenon. NO emission increases after P-DPF because of the elevated combustion temperature due to the injection of more fuel, indicating a rise of 3% and 7% when using B10 and B100, respectively.

The analyzed test results of emission factors under NEDC show that total HC and CO decrease with the introduction of P-DPF. This can be due to the support of catalytic coating that forms CO_2 and water in the reactions of HC and CO with O_2. As a result, the use of P-DPF fueled with B10 reduces total HC by 22% and CO by 20%, while the combination with B100 reduces them by 14% and 13%, respectively. However, a slight NOx reduction is observed when P-DPF is installed downstream of the exhaust system, ranging from 7% - 9%. This can be attributed to the conversion of NO to NO_2 through a reaction with excess O_2, and the use of NO_2 as an oxidizing agent to convert soot to CO_2 at temperatures as low as 250°C.

Biodiesel proves to be an effective solution for reducing particulate emissions, lowering PN by 45% and PM mass by 32% in vehicle exhaust compared to commercial fuel B10. However, increasingly stringent emission regulations may require an even more effective approach. A partial-flow P-DPF can be a practical solution when combined with biodiesel to reduce harmful emissions from diesel vehicles. The use of P-DPF with B10 and B100 results in significant PN reduction, exhibiting 36% and 39%, respectively. Furthermore, more than 59% of PM mass is reduced by P-DPF for both fuels, with a slight advantage for biodiesel B100 at 60%. This significant PM reduction is attributed to the alternately clogged channels at the outlet that allow the exhaust gases to pass through while trapping PM inside porous walls. Additionally, simultaneous trapping and passive oxidation of soot may occur by utilizing NO_2 and O_2 as oxidizing agents to convert soot to CO_2 at temperatures above 250°C and 350°C, respectively.

Installing P-DPF downstream of the exhaust system significantly reduces regulated emissions while having a negligible impact on fuel flow rate and brake thermal efficiency. This demonstrates the effectiveness of the approach in reducing harmful emissions from untreated diesel vehicles with minimal modifications. However, further research is needed to obtain a comprehensive evaluation of the impact of P-DPF on vehicle performance and emissions. It is beneficial to establish a baseline for the P-DPF performance analysis by comparing the results with a full-flow DPF. In-cylinder pressure and temperature are also essential parameters for understanding the effect of backpressure from P-DPF installation on combustion characteristics and emissions. Additionally, the effect of different porosities on backpressure, vehicle performance, and emissions reduction should be investigated to optimize porosity. The partial soot oxidation within P-DPF at low exhaust temperatures can be further studied to better understand the filter's passive regeneration. Moreover, the P-DPF’s filtration behavior and its effect on backpressure during a long-term operation should be examined. Finally, microscopic visualization of particulate matter trapped on the paper filter could provide more reliable results when using a consistent filter substrate. These thorough investigations are necessary for a comprehensive evaluation of P-DPF feasibility.

REFERENCES

[1] Majewski, W. A., & Khair, M. K. (2006). *Diesel Emissions and Their Control*. SAE International.

[2] Kagawa, J. (2002). Health effects of diesel exhaust emissions—a mixture of air pollutants of worldwide concern. *Toxicology*.

[3] Lloyd, A. C., & Cackette, T. A. (2001). Diesel engines: environmental impact and control. *J Air Waste Manag Assoc, 51*(6), 809-847.

[4] Reşitoğlu, İ. A., Altinişik, K., & Keskin, A. (2014). The pollutant emissions from diesel-engine vehicles and exhaust aftertreatment systems. *Clean Technologies and Environmental Policy, 17*(1), 15-27.

[5] IEA. (2023). *Global EV Outlook 2023*. IEA.

[6] Zhang, Z., Li, J., Tian, J., et al. (2022). Performance, combustion and emission characteristics investigations on a diesel engine fueled with diesel/ ethanol /n-butanol blends. *Energy, 249*.

[7] Zhu, L., Cheung, C. S., Zhang, W. G., et al. (2011). Combustion, performance and emission characteristics of a DI diesel engine fueled with ethanol–biodiesel blends. *Fuel, 90*(5), 1743-1750.

[8] Ramadhas, A. S., Jayaraj, S., & Muraleedharan, C. (2004). Use of vegetable oils as I.C. engine fuels—A review. *Renewable Energy, 29*(5), 727-742.

[9] R. Prasad, V. R. B. (2010). A Review on Diesel Soot Emission, its Effect and Control. *Bulletin of Chemical Reaction Engineering & Catalysis, 5*(2), 69-86.

[10] Teske, S., Bratzel, S., Tellermann, R., et al. (2022). Net Zero: The Remaining Global Market Volume for Internal Combustion Engines in Light-Duty Vehicles under a 1.5 °C Carbon Budget Trajectory. *Energies, 15*(21).

[11] Leach, F., Kalghatgi, G., Stone, R., et al. (2020). The scope for improving the efficiency and environmental impact of internal combustion engines. *Transportation Engineering, 1*.

[12] Wu, C.-W., Chen, R.-H., Pu, J.-Y., et al. (2004). The influence of air–fuel ratio on engine performance and pollutant emission of an SI engine using ethanol–gasoline-blended fuels. *Atmospheric Environment, 38*(40), 7093-7100.

[13] Faiz, A., Weaver, C. S., & Walsh, M. P. (1996). *Air Pollution from Motor Vehicles Standards and Technologies for Controlling Emissions*. The World Bank, Washington.

[14] Luo, X., Yu, X., Zha, K., et al. (2014). In-Cylinder Wall Temperature Influence on Unburned Hydrocarbon Emissions During Transitional Period in an Optical Engine Using a Laser-Induced Phosphorescence Technique. *SAE International Journal of Engines, 7*(2), 995-1002.

[15] Sakai, H., Sato, S., Mori, S., et al. (2020). Analysis of Unburned Hydrocarbon Generated from Wall under Lean Combustion. *SAE Technical Paper 2020-01-0295*.

[16] Palash, S. M., Kalam, M. A., Masjuki, H. H., et al. (2013). Impacts of biodiesel combustion on NOx emissions and their reduction approaches. *Renewable and Sustainable Energy Reviews, 23*, 473-490.

[17] Varatharajan, K., & Cheralathan, M. (2012). Influence of fuel properties and composition on NOx emissions from biodiesel powered diesel engines: A review. *Renewable and Sustainable Energy Reviews, 16*(6), 3702-3710.

[18] Tree, D. R., & Svensson, K. I. (2007). Soot processes in compression ignition engines. *Progress in Energy and Combustion Science, 33*(3), 272-309.

[19] Bruce, C. W., Stromberg, T. F., Gurton, K. P., et al. (1991). Trans-spectral absorption and scattering of electromagnetic radiation by diesel soot. *Applied Optics, 30*(12), 1537-1546.

[20] Pinson, J. A., Ni, T., & Litzinger, T. A. (1994). Quantitative Imaging Study of the Effects of Intake Air Temperature on Soot Evolution in an Optically-Accessible D.I. Diesel Engine. *SAE Technical Paper 942044*.

[21] Tree, D. R., & Foster, D. E. (1994). Optical Measurements of Soot Particle Size, Number Density, and Temperature in a Direct Injection Diesel Engine as a Function of Speed and Load. *SAE Technical Paper 940270*.

[22] Lee, K. O., Cole, R., Sekar, R., et al. (2001). Detailed Characterization of Morphology and Dimensions of Diesel Particulates via Thermophoretic Sampling. *SAE Technical Paper 2001-01-3572*.

[23] Ladommatos, N., & Zhao, H. (1994). A Guide to Measurement of Flame Temperature and Soot Concentration in Diesel Engines Using the Two-Colour Method Part I Principles. *SAE Technical Paper 941956*.

[24] Kittelson, D. B. (1998). ENGINES AND NANOPARTICLES: A REVIEW. *Journal of Aerosol Science, 29*(5-6), 575-588.

[25] Matti Maricq, M. (2007). Chemical characterization of particulate emissions from diesel engines A review. *Journal of Aerosol Science, 38*(11), 1079-1118.

[26] Kleinová, A., Vailing, I., Lábaj, J., et al. (2011). Vegetable oils and animal fats as alternative fuels for diesel engines with dual fuel operation. *Fuel Processing Technology, 92*(10), 1980-1986.

[27] Franco, Z., & Nguyen, Q. D. (2011). Flow properties of vegetable oil–diesel fuel blends. *Fuel, 90*(2), 838-843.

[28] Hu, J., Du, Z., Li, C., et al. (2005). Study on the lubrication properties of biodiesel as fuel lubricity enhancers. *Fuel, 84*(12-13), 1601-1606.

[29] Geller, D. P., & Goodrum, J. W. (2004). Effects of specific fatty acid methyl esters on diesel fuel lubricity. *Fuel, 83*(17-18), 2351-2356.

[30] Buyukkaya, E. (2010). Effects of biodiesel on a DI diesel engine performance, emission and combustion characteristics. *Fuel, 89*(10), 3099-3105.

[31] Nguyen, V. H., Duong, M. Q., Nguyen, K. T., et al. (2020). An Extensive Analysis of Biodiesel Blend Combustion Characteristics under a Wide-Range of Thermal Conditions of a Cooperative Fuel Research Engine. *Sustainability, 12*(18).

[32] Canakci, M. (2007). Combustion characteristics of a turbocharged DI compression ignition engine fueled with petroleum diesel fuels and biodiesel. *Bioresour Technol, 98*(6), 1167-1175.

[33] Can, Ö. (2014). Combustion characteristics, performance and exhaust emissions of a diesel engine fueled with a waste cooking oil biodiesel mixture. *Energy Conversion and Management, 87*, 676-686.

[34] Russell, A., & Epling, W. S. (2011). Diesel Oxidation Catalysts. *Catalysis Reviews, 53*(4), 337-423.

[35] Khair, M. K. (2003). A Review of Diesel Particulate Filter Technologies. *SAE Technical Paper 2003-01-2303*.

[36] Guan, B., Zhan, R., Lin, H., et al. (2015). Review of the state-of-the-art of exhaust particulate filter technology in internal combustion engines. *J Environ Manage, 154*, 225-258.

[37] Zhang, Y., Lou, D., Tan, P., et al. (2023). Effect of catalyzed diesel particulate filter and its catalyst loading on emission characteristics of a non-road diesel engine. *J Environ Sci (China), 126*, 794-805.

[38] Yamamoto, K., & Sakai, T. (2015). Simulation of continuously regenerating trap with catalyzed DPF. *Catalysis Today, 242*, 357-362.

[39] Orihuela, M. P., Chacartegui, R., Gómez-Martín, A., et al. (2020). Performance trends in wall-flow diesel particulate filters: Comparative analysis of their filtration efficiency and pressure drop. *Journal of Cleaner Production, 260*.

[40] Ohara, E., Mizuno, Y., Miyairi, Y., Mizutani, T. et al. (2007). Filtration Behavior of Diesel Particulate Filters (1). *SAE Technical Paper 2007-01-0921*.

[41] Shuji Fujii, T. A. (2011). Design Optimization of Non-Catalyzed DPF from Viewpoint of Back Pressure in Ash loading State. *SAE Technical Paper 2011-01-2091*.

[42] Ebrahimnataj, M. R., Tiji, A. E., Eisapour, M., et al. (2021). The effect of soot accumulation and backpressure of an integrated after-treatment system on diesel engine performance. *Journal of Thermal Analysis and Calorimetry, 147*(15), 8435-8443.

[43] Ingo Mikulic, R. Z., Scott Eakle. (2010). Dependence of Fuel Consumption on Engine Backpressure Generated by a DPF. *SAE Technical Paper 2010-01-0535*.

[44] Görsmann, C. (2005). Catalytic Coatings for Active and Passive Diesel Particulate Filter Regeneration. *Monatshefte für Chemie, 136*(1), 91-105.

[45] Vora, K. C., Gurnule, K. E., & Venkatesh, S. (2020). Diesel Particulate Filter. In *Design and Development of Heavy Duty Diesel Engines* (pp. 313-339). Springer.

[46] Pavel Farafontov, J. M., Shazam Williams. (2007). Optimization of Partial Filter Technology for diesel engines. *SAE Technical Paper 2007-01-4025*.

[47] Brück, R., Hirth, P., Reizig, M., et al. (2001). Metal Supported Flow-Through Particulate Trap; a Non-Blocking Solution.

[48] Isaline, L., Jose, H., & Athanasios, T. (2014). The Use of a Partial Flow Filter to Assist the Diesel Particulate Filter and Reduce Active Regeneration Events. *SAE International Journal of Engines, 7*(4), 1953-1960.

[49] Jacobs, T., Chatterjee, S., Conway, R., et al. (2006). Development of Partial Filter Technology for HDD Retrofit. *SAE Technical Paper 2006-01-0213*.

[50] Kramer, J., Pfahl, U., Bruestle, C., et al. (2009). The PM-Metalit A PM control technology for Tier 4 Off-Highway Applications. *SAE Technical Paper 2009-01-2838*.

[51] Mon Phyo, M. Z., Wai, P., Thin, M. H., et al. (2023). Experimental investigation of metallic partial-flow particulate filter on a diesel engine's combustion pressure and particle emission. *Case Studies in Thermal Engineering, 49*.

[52] Oh, B.-s., Thaeviriyakul, P., Phairote, W., et al. (2023). Effect of Metallic Microfiber Flow Through Diesel Particulate Filter System on Diesel Engine's Particle Emission Physicochemical Characteristics. *Emission Control Science and Technology, 9*(1), 47-65.

[53] Dang, Q. H., Karin, P., Cosh, P. T., et al. (2024). *Impact of Partial-Flow Particulate Filter on Emissions from a Light-Duty Diesel Vehicle*. 13th TSME International Conference on Mechanical Engineering, Thailand.

[54] Jain, S., & Sharma, M. P. (2010). Prospects of biodiesel from Jatropha in India: A review. *Renewable and Sustainable Energy Reviews, 14*(2), 763-771.

[55] Mizutani, T., Kaneda, A., Ichikawa, S., Miyairi, Y. et al. (2007). Filtration Behavior of Diesel Particulate Filters (2). *SAE Technical Paper 2007-01-0923*.

[56] ASTM C373-88, Standard Test Method for Water Absorption, Bulk Density, Apparent Porosity, and Apparent Specific Gravity of Fired Whiteware Products. (2006). In West Conshohocken, PA: ASTM International.

[57] Heywood, J. B. (2019). *Internal Combustion Engine Fundamentals*. McGraw-Hill.

[58] Kong, X., Li, Z., Shen, B., et al. (2019). Simulation of flow and soot particle distribution in wall-flow DPF based on lattice Boltzmann method. *Chemical Engineering Science, 202*, 169-185.

[59] Banjuraizah, J., Mohamad, H., & Ahmad, Z. A. (2011). Effect of Excess MgO Mole Ratio in a Stoichiometric Cordierite (2MgO·2Al2O3·5SiO2) Composition on the Phase Transformation and Crystallization Behavior of Magnesium Aluminum

Silicate Phases. *International Journal of Applied Ceramic Technology, 8*(3), 637-645.

[60] Maier, N., Nickel, K. G., Engel, C., et al. (2010). Mechanisms and orientation dependence of the corrosion of single crystal Cordierite by model diesel particulate ashes. *Journal of the European Ceramic Society, 30*(7), 1629-1640.

[61] Devaiah, D., Reddy, L. H., Park, S.-E., et al. (2018). Ceria–zirconia mixed oxides: Synthetic methods and applications. *Catalysis Reviews, 60*(2), 177-277.

[62] Léonard, F., Lange, A., Kupsch, A., et al. (2021). On the Morphological and Crystallographic Anisotropy of Diesel Particulate Filter Materials. *Advanced Engineering Materials, 24*(6).

[63] Onel, Y., Lange, A., Staude, A., et al. (2013). Evaluating Porosity in Cordierite Diesel Particulate Filter Materials Part 2 Statistical Analysis of Computed Tomography Data. *Journal of ceramic science and technology, 5*(1), 10.

[64] Canakci, M., Erdil, A., & Arcaklioğlu, E. (2006). Performance and exhaust emissions of a biodiesel engine. *Applied Energy, 83*(6), 594-605.

[65] Muralidharan, K., & Vasudevan, D. (2011). Performance, emission and combustion characteristics of a variable compression ratio engine using methyl esters of waste cooking oil and diesel blends. *Applied Energy, 88*(11), 3959-3968.

[66] Pramanik, K. (2003). Properties and use of jatropha curcas oil and diesel fuel blends in compression ignition engine. *Renewable Energy, 28*(2), 239-248.

[67] Ramadhas, A. S., Muraleedharan, C., & Jayaraj, S. (2005). Performance and emission evaluation of a diesel engine fueled with methyl esters of rubber seed oil. *Renewable Energy, 30*(12), 1789-1800.

[68] Pandey, R. K., Rehman, A., & Sarviya, R. M. (2012). Impact of alternative fuel properties on fuel spray behavior and atomization. *Renewable and Sustainable Energy Reviews, 16*(3), 1762-1778.

[69] Wai, P., Kanokkhanarat, P., Oh, B.-S., et al. (2022). Experimental investigation of the influence of ethanol and biodiesel on common rail direct injection diesel Engine's combustion and emission characteristics. *Case Studies in Thermal Engineering, 39*.

[70] R. M. Olree, D. L. L. (1984). Diesel combustion cetane number effects. *SAE Technical Paper 840108*.

[71] Grigoratos, T., Fontaras, G., Giechaskiel, B., et al. (2019). Real world emissions performance of heavy-duty Euro VI diesel vehicles. *Atmospheric Environment, 201*, 348-359.

[72] Bakeas, E., Karavalakis, G., Fontaras, G., et al. (2011). An experimental study on the impact of biodiesel origin on the regulated and PAH emissions from a Euro 4 light-duty vehicle. *Fuel, 90*(11), 3200-3208.

[73] Al-Shemmeri, T. T., & Oberweis, S. (2011). Correlation of the NOx emission and exhaust gas temperature for biodiesel. *Applied Thermal Engineering, 31*(10), 1682-1688.

[74] Nabi, M. N., Rasul, M. G., Arefin, M. A., et al. (2021). Investigation of major factors that cause diesel NOx formation and assessment of energy and exergy parameters using e-diesel blends. *Fuel, 292*.

[75] Magín Lapuerta, O. A. a. R. B. (2002). Diesel Particulate Emissions from Biofuels Derived from Spanish Vegetable Oils. *SAE Technical Paper 2002-01-1657*.

[76] Robertson, P. (2023). *Bangkok Air Quality – Live Bangkok, Thailand AQI and PM2.5 Readings*. Retrieved 25 March 2024 from https://smartairfilters.com/en/blog/bangkok-thailand-live-aqi-air-quality/

[77] ChooChuay, C., Pongpiachan, S., Tipmanee, D., et al. (2020). Impacts of PM2.5 sources on variations in particulate chemical compounds in ambient air of Bangkok, Thailand. *Atmospheric Pollution Research, 11*(9), 1657-1667.

Appendix A

FUEL PROPERTIES AND COMPOSITIONS

A-01. Properties of Fuel B10

FOCUSLAB Fluid & Oil Analysis Technology

ISO 9001 : 2015 Certified

Focuslab Ltd

Customer Code	:	20010	Sample Information	
Customer Name	:	KMITL	Unit ID / Sample Information Identification	: B10
Address	:	3 Moo 2, Chalongkrung Road Ladkrabang Bangkok 10520	Unit type	: FUEL
			Oil type	: DIESEL B10
			Sampling Date	: 22-Jun-21
			Recieved Date	: 22-Jun-21
Test Code	:	811A		

Test Report Sample No 21063747

Test Description	Test Method	Test Result	Limit (a)
Apperance			
Color	Visual Inspection	Bright and Clear	Bright and Clear
Diesel Fuel			
Density at 15 C , g/cm^3	ASTM D4052	0.835	0.81 - 0.87
Cetane Index	ASTM D976	54.9	Min 50
Distillation , C	ASTM D86		
Initial Boiling Point		180.0	-
90%vol. Recovered		344.2	Max 357
Flash Point	ASTM D93	66.0	Min 52
Fatty Acid Methyl Ester, %vol	EN 14078	10.2	9 - 10
Pour Point , °C	ASTM D97	0.0	Max 10
Flow Properties			
Viscosity at 40 C , cSt	ASTM D445	3.0	1.8 - 4.1
Cleanliness			
Total Contamination , mg/kg	EN 12662	6.2	Max 24.0
Micro Carbon Residue (MCR) , %mass	ASTM D4530	<0.01	Max 0.3
Ash , %wt	ASTM D482	<0.001	Max 0.010
Total Sulfur Content , mg/kg	ASTM D5453	24.4	Max 50
Water Content , mg/kg	ASTM D6304	691	Max 200
Water and Sediment , %Vol.	ASTM D2709	<0.01	Max 0.05

Interpretation of the Test Result
- Test results are based on received fuel sample , submitted and identified by client.
- Data is provided above.

Recommendation
- No recommendation for R&D.

Remark
(a) Diesel fuel is from Thailand Diesel Specification - MOE - 2563

Tested and Issued By

Kanjana K.
Lab Technologist

Approved and Authorised by

Somchai J.
Machine Lubricant Analyst

2/57 Bangna Complex Office Tower, 12 th Fl , Soi Bangna- Trad 25, North Bangna, Bangna, Bangkok 10260, Thailand
http://www.focuslab.co.th
Tel : (66 2) 3618600-3 Fax : (66 2) 3618567

FL-6.7

(continued)

FOCUSLAB™ Fluid & Oil Analysis Technology

ISO 9001 : 2015 Certified

Focuslab Ltd

Customer Code	:	20010
Customer Name	:	KMITL
Address	:	3 Moo 2, Chalongkrung Road Ladkrabang Bangkok 10520
Test Code	:	811A

Sample Information

Unit ID / Sample Information Identification	:	**B10**
Unit type	:	FUEL
Oil type	:	not given
Sampling Date	:	22-Jun-21
Recieved Date	:	22-Jun-21

B10 | Good and Qualified Diesel Fuel

2/57 Bangna Complex Office Tower, 12 th Fl , Soi Bangna- Trad 25, North Bangna, Bangna, Bangkok 10260, Thailand
http://www.focuslab.co.th
Tel : (66 2) 3618600-3 Fax : (66 2) 3618567

FL-6.7

A-02. Properties of Biodiesel

บริษัท น้ำมันพืชปทุม จำกัด
PATUM VEGETABLE OIL CO.,LTD.

แบบฟอร์ม ใบแจ้งผลการวิเคราะห์ ตัวอย่างน้ำมันไบโอดีเซล

CERTIFICATE OF ANALYSIS

Reference Material for Fatty Acid Methyl Ester

Attention	:	รศ.ดร.ปรีชา การินทร์
	:	สถาบันเทคโนโลยีพระจอมเกล้าเจ้าคุณทหารลาดกระบัง
Product Name	:	Biodiesel (Fatty Acid Methyl Ester)
Date of Delivery	:	July 11, 2023
Remark	:	Sample should be stored out of direct sunlight, and preferably at or below 30 °C

ANALYSIS RESULT

	Test Parameter	Limitation	Test Method	Result
1	Methyl Ester, %wt	96.5 Min	EN 14103	98.1
2	Density at 30°C, kg/m^3	860 – 900	ASTM D 1298	863.4
3	Viscosity at 40°C, cSt	3.5 – 5.0	ASTM D 445	4.5
4	Flash Point, °C	120 Min	ASTM D 93	> 120
5	Water, mg/kg	500 Max	EN ISO 12937	230
6	Oxidation Stability at 110°C, hr.	10 Min	EN 15751	32.3
7	Acid Value, mgKOH/g	0.50 Max	ASTM D 664	0.19
8	Iodine Value, gI_2/100 g	120 Max	EN 14111	44.7
9	Linolenic Acid Methyl Ester, %wt	12.0 Max	EN 14103	0.16
10	Methanol, %wt	0.20 Max	EN 14110	0.01
11	Monoglyceride, %wt	0.40 Max	EN 14105	0.33
12	Diglyceride, %wt	0.20 Max	EN 14105	0.04
13	Triglyceride, %wt	0.20 Max	EN 14105	0.00
14	Free Glycerin, %wt	0.02 Max	EN 14105	0.00
15	Total Glycerin, %wt	0.25 Max	EN 14105	0.09
16	Group I metals (Na+K) , mg/kg	5.0 Max	EN 14538	<1.00
	Group II metals (Ca+Mg), mg/kg	5.0 Max	EN 14538	<1.00
17	Phosphorus, %wt	0.0010 Max	EN 14107	<0.0001
18	Additive	Report	-	No
19	Appearance	Clear	Visual	Clear
20	Cloud Point : CP, °C	Report	ASTM D 2500	15.4
21	Cold Filter Plugging Point : CFPP, °C	Report	ASTM D 6371	13.4

Tested by : _____ (Quality Control Officer)

Approved by : _____ (Quality Control Supervisor)

QUALITY CONTROL OLEOCHEMICAL – LABORATORY SECTION

OFF: 1/8 CHARANSNITWONGS RD. SOI 55 BANGPLAD BANGKOK 10700 THAILAND. TELEX: 82431 PATUM TH
TEL. 66 (02) 434-8384-7 FAX: 66 (02) 433-6423
FAC: TEL 66 (02) 581-5211, 581-5763, 581-2348 FAX: 66 (02) 581-6407

(continued)

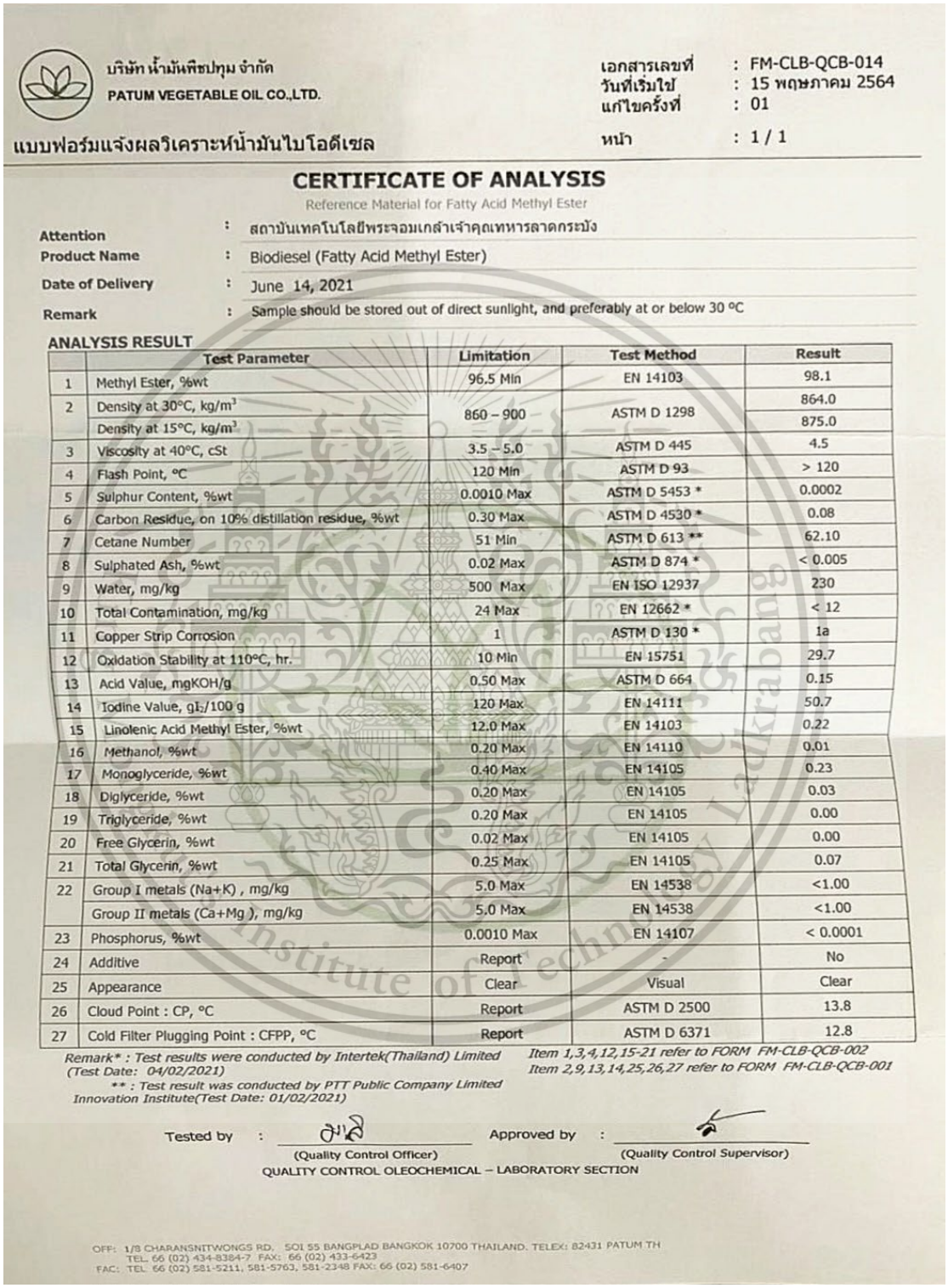

บริษัท น้ำมันพืชปทุม จำกัด
PATUM VEGETABLE OIL CO.,LTD.

เอกสารเลขที่ : FM-CLB-QCB-014
วันที่เริ่มใช้ : 15 พฤษภาคม 2564
แก้ไขครั้งที่ : 01
หน้า : 1 / 1

แบบฟอร์มแจ้งผลวิเคราะห์น้ำมันไบโอดีเซล

CERTIFICATE OF ANALYSIS

Reference Material for Fatty Acid Methyl Ester

Attention : สถาบันเทคโนโลยีพระจอมเกล้าเจ้าคุณทหารลาดกระบัง
Product Name : Biodiesel (Fatty Acid Methyl Ester)
Date of Delivery : June 14, 2021
Remark : Sample should be stored out of direct sunlight, and preferably at or below 30 °C

ANALYSIS RESULT

	Test Parameter	Limitation	Test Method	Result
1	Methyl Ester, %wt	96.5 Min	EN 14103	98.1
2	Density at 30°C, kg/m³	860 – 900	ASTM D 1298	864.0
	Density at 15°C, kg/m³			875.0
3	Viscosity at 40°C, cSt	3.5 – 5.0	ASTM D 445	4.5
4	Flash Point, °C	120 Min	ASTM D 93	> 120
5	Sulphur Content, %wt	0.0010 Max	ASTM D 5453 *	0.0002
6	Carbon Residue, on 10% distillation residue, %wt	0.30 Max	ASTM D 4530 *	0.08
7	Cetane Number	51 Min	ASTM D 613 **	62.10
8	Sulphated Ash, %wt	0.02 Max	ASTM D 874 *	< 0.005
9	Water, mg/kg	500 Max	EN ISO 12937	230
10	Total Contamination, mg/kg	24 Max	EN 12662 *	< 12
11	Copper Strip Corrosion	1	ASTM D 130 *	1a
12	Oxidation Stability at 110°C, hr.	10 Min	EN 15751	29.7
13	Acid Value, mgKOH/g	0.50 Max	ASTM D 664	0.15
14	Iodine Value, gI₂/100 g	120 Max	EN 14111	50.7
15	Linolenic Acid Methyl Ester, %wt	12.0 Max	EN 14103	0.22
16	Methanol, %wt	0.20 Max	EN 14110	0.01
17	Monoglyceride, %wt	0.40 Max	EN 14105	0.23
18	Diglyceride, %wt	0.20 Max	EN 14105	0.03
19	Triglyceride, %wt	0.20 Max	EN 14105	0.00
20	Free Glycerin, %wt	0.02 Max	EN 14105	0.00
21	Total Glycerin, %wt	0.25 Max	EN 14105	0.07
22	Group I metals (Na+K) , mg/kg	5.0 Max	EN 14538	<1.00
	Group II metals (Ca+Mg), mg/kg	5.0 Max	EN 14538	<1.00
23	Phosphorus, %wt	0.0010 Max	EN 14107	< 0.0001
24	Additive	Report	-	No
25	Appearance	Clear	Visual	Clear
26	Cloud Point : CP, °C	Report	ASTM D 2500	13.8
27	Cold Filter Plugging Point : CFPP, °C	Report	ASTM D 6371	12.8

Remark : Test results were conducted by Intertek(Thailand) Limited (Test Date: 04/02/2021)*
*** : Test result was conducted by PTT Public Company Limited Innovation Institute(Test Date: 01/02/2021)*

Item 1,3,4,12,15-21 refer to FORM FM-CLB-QCB-002
Item 2,9,13,14,25,26,27 refer to FORM FM-CLB-QCB-001

Tested by : _____ (Quality Control Officer)
Approved by : _____ (Quality Control Supervisor)
QUALITY CONTROL OLEOCHEMICAL – LABORATORY SECTION

OFF: 1/8 CHARANSNITWONGS RD. SOI 55 BANGPLAD BANGKOK 10700 THAILAND. TELEX: 82431 PATUM TH
TEL. 66 (02) 434-8384-7 FAX: 66 (02) 433-6423
FAC: TEL. 66 (02) 581-5211, 581-5763, 581-2348 FAX: 66 (02) 581-6407

A-03. Bomb Calorimeter Test Results

Analysis Report

Sample	Biodiesel
Sample owner	King Mongkut's Institute of Technology Ladkrabang
Objective	To analyse heating value of combustion
Instrument	Automatic Bomb Calorimeter ; Leco model AC - 500
Job ID	640707-9246
Analysis Date	July 28, 2021

Results

Sample name	Heating value of combustion (MJ/kg)		
	#1	#2	Average
Biodiesel B7	45.26	45.24	45.25
Biodiesel B10	45.80	45.46	45.63
Biodiesel B20	44.89	45.01	44.95
Biodiesel B100	39.84	40.03	39.94
Biodiesel B20E5	43.90	43.99	43.95
Biodiesel B20E10	42.66	42.78	42.72
Biodiesel B20E20	40.61	40.45	40.53

(Mrs. Aree Limnirandorn)

Analyst

A-04. Chemical Composition Test Results

EagerSmart

Method name : CHNS
Method filename : E:\...\65-002\CHNS.mth

Detection and integration parameters

Time base : (s)
Peak width : 10
Peak threshold : 1
Minimum area : 1500
Skim ratio : 10
Next sample to acquire : 19
Real time plot scale : 10
Real time plot offset : 0

Time events table

#	Time	Events type	New value
1	.1	Disable integration	
2	35	Enable integration	
3	160	Change peak threshold	.1
4	160	Change skim ratio	1
5	160	Change peak width	40
6	500.3922	Disable integration	

Calculation and report parameters

Calibration method : Linear fit
Heat Value calc. : No
CO2 Emission Factor calc. : No
Protein calc. : No
Report on : None
Peak option : Only calibrated peaks
Report format : Default
Report publisher : No
Calibration report : Yes
Concentration unit :
Stripchart format : None
Autoscalling : ---
Stripchart full scale : 10
Stripchart scale offset : 0
Stripchart initial time : 0
Stripchart end time : 600
Append for summarize : Element %
Signal to noise report : Yes
Signal peak name :
Noise evaluation from/to : 0.0-0.0(s):

(continued)

Custom report

Component table

#	Component name	Ret.T.	Window	Min. %	Max.%
1	Nitrogen	47	10		
2	Carbon	67	14		
3	Hydrogen	194	60		
4	Sulphur	412	88		

Calibration factors

#	Component name	Kb	Kc
1	Nitrogen	1995673	0
2	Carbon	4763351	0
3	Hydrogen	1.488643E+07	0
4	Sulphur	2078495	0

Standard table

Sample Num.4 Sample name: STD1 (BBOT 1.5 mg)
Filename: File004 STD1 (BBOT 1_5 mg) Std name: BBOT

#	Component name	Concentration	Valid
1	Nitrogen	6.53	Yes
2	Carbon	72.58	Yes
3	Hydrogen	6.1	Yes
4	Sulphur	7.41	Yes

Sample Num.5 Sample name: STD2 (BBOT 2 mg)
Filename: File005 STD2 (BBOT 2 mg) Std name: BBOT

#	Component name	Concentration	Valid
1	Nitrogen	6.53	Yes
2	Carbon	72.58	Yes
3	Hydrogen	6.1	Yes
4	Sulphur	7.41	Yes

Sample Num.6 Sample name: STD3 (BBOT 2.5 mg)
Filename: File006 STD3 (BBOT 2_5 mg) Std name: BBOT

#	Component name	Concentration	Valid
1	Nitrogen	6.53	Yes
2	Carbon	72.58	Yes
3	Hydrogen	6.1	Yes
4	Sulphur	7.41	Yes

Sample Num.7 Sample name: STD4 (BBOT 3 mg)
Filename: File007 STD4 (BBOT 3 mg) Std name: BBOT

#	Component name	Concentration	Valid
1	Nitrogen	6.53	Yes
2	Carbon	72.58	Yes
3	Hydrogen	6.1	Yes
4	Sulphur	7.41	Yes

Operator ID/info

Operator ID :
Company name :
Column type :
Column lenght :
Date packing :
Comment :

(continued)

(continued)

(continued)

(continued)

(Continued)

EagerSmart Summarize Results

Date : 11/08/2021 at 15:52:41
Method Name : CHNS
Method Filename : CHNS.mth

Group No : 1 Sample Name	Element % Nitrogen	Carbon	Hydrogen	Sulphur
B100_1	0	76.40828705	12.38687801	0
B100_4	0	77.04006958	12.53007603	0
B20_2	0	82.24542999	13.38155937	0
B20_3	0	82.98455048	13.52551937	0
B10_1	0	84.58450317	13.53221703	0
B10_2	0	84.74507141	13.58557034	0

6 Sample(s) in Group No : 1

Component Name	Average	Std. Dev.	% Rel. S. D.	Variance
Nitrogen	0	0.00000	0.0000	0.0000
Carbon	81.33465195	3.70018	4.5493	13.6913
Hydrogen	13.15697002	0.54714	4.1586	0.2994
Sulphur	0	0.00000	0.0000	0.0000

EagerSmart Summarize Results

Date : 11/08/2021 at 15:52:55
Method Name : CHNS
Method Filename : CHNS.mth

Group No : 1 Sample Name	Element % Nitrogen	Carbon	Hydrogen	Sulphur
B100_2	0.05251986906	76.13822174	0	0
B100_3	0.04693116993	76.21728516	0	0

2 Sample(s) in Group No : 1

Component Name	Average	Std. Dev.	% Rel. S. D.	Variance
Nitrogen	0.04972551949	0.00395	7.9472	0.0000
Carbon	76.17775345	0.05591	0.0734	0.0031
Hydrogen	0	0.00000	0.0000	0.0000
Sulphur	0	0.00000	0.0000	0.0000

Appendix B

ELEMENTAL COMPOSITION RESULTS

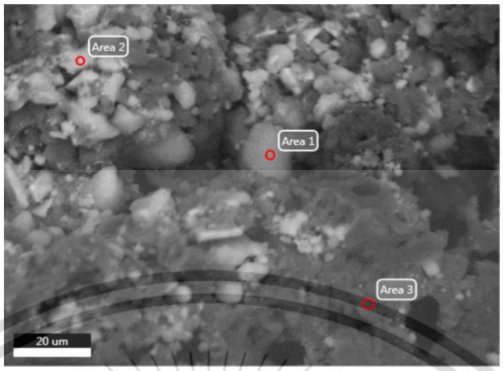

EDS Area1

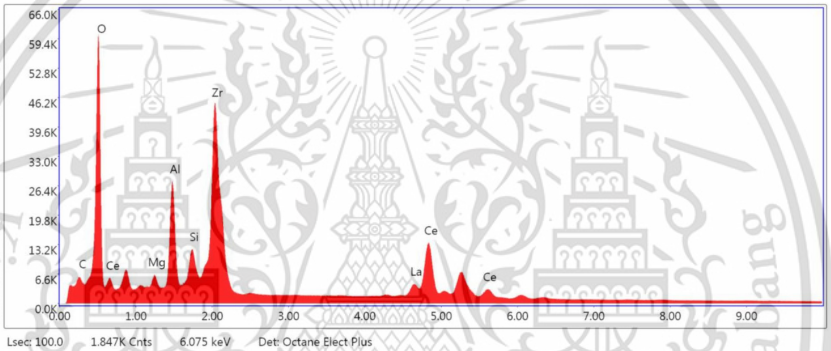

Element	Weight %
C	3.95
O	20.05
Mg	1.29
Al	7.01
Si	2.83
Zr	29.62
La	6.84
Ce	28.41

(continued)

EDS Area2

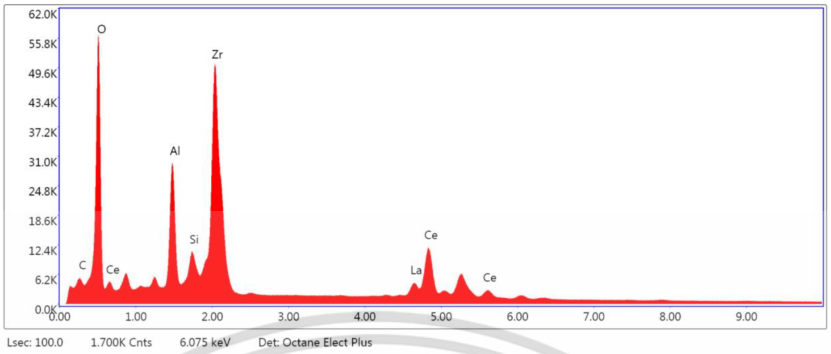

Element	Weight %
C	3.54
O	19.92
Al	7.74
Si	2.53
Zr	33.90
La	7.28
Ce	25.09

EDS Area3

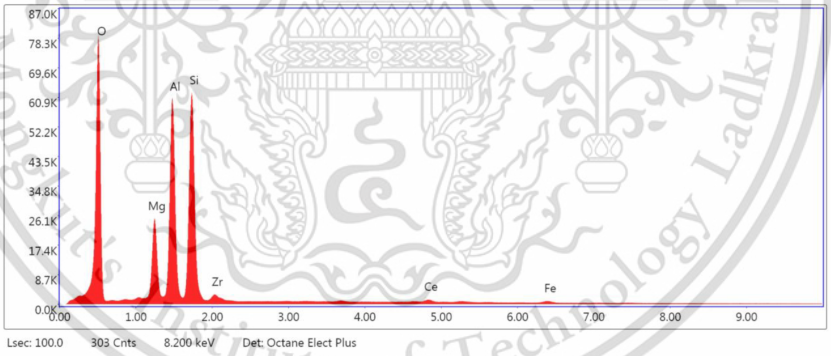

Element	Weight %
O	34.17
Mg	8.55
Al	23.22
Si	26.14
Zr	1.75
Ce	4.65
Fe	1.52

Appendix C

CONFERENCE PARTICIPATION

The 13th TSME International Conference on Mechanical Engineering
12th – 15th December 2023
Chiang Mai, Thailand

TSME ICOME 2023
Reaching Sustainable Development Goals

AEC0019

Impact of Partial-Flow Particulate Filter on Emissions from a Light-Duty Diesel Vehicle

Huy Quang Dang[1,2], Preechar Karin[1,*], Plan Teekatasn Cosh[1], Poonnut Thaeviriyakul[1], Pongsak Kummul[1], Sompong Srimanosaowapak[3], Hidenori Kosaka[4], and Mek Srilomsak[1]

[1]School of Engineering, King Mongkut's Institute of Technology Ladkrabang, Bangkok 10520, Thailand
[2]College of Engineering, Can Tho University, Can Tho, Vietnam
[3]National Metal and Materials Technology Center, National Science and Technology Development Agency, Pathum Thani 12120, Thailand
[4]School of Engineering, Tokyo Institute of Technology, Tokyo 152-8552, Japan

* Corresponding Author: preechar.ka@kmitl.ac.th

Abstract. This study examines particle and gaseous emissions from a light-duty diesel vehicle equipped with a partial-flow catalyzed diesel particulate filter (P-CDPF). The vehicle underwent testing on a chassis dynamometer following the new European driving cycle. The results show a significant reduction in total hydrocarbon (THC) and carbon monoxide (CO) when employing P-CDPF. Specifically, catalytic coating successfully converted 48% of THC and 66% of CO into carbon dioxide (CO_2). This resulted in a 6% increment in CO_2 emissions after the driving cycles. Nitrogen oxides (NOx) increased after P-CDPF because of elevated in-cylinder temperature due to backpressure. Additionally, the integration of P-CDPF resulted in a 45% reduction in particulate number (PN) and a 60% reduction in particulate mass (PM). The findings of this study propose a feasible solution for controlling harmful substances, thereby contributing significantly to practical initiatives aimed at reducing harmful emissions emitted by untreated diesel vehicles.

Keywords: Diesel Emission, Particulate Matter, Partial Flow Diesel Particulate Filter, New European Driving Cycle.

1. Introduction

Diesel engine has been widely used in various fields of road transportation, agriculture, and industry due to its high efficiency [1]. However, it releases highly toxic gases that directly affect human health and the environment [2-4]. The ideal products of diesel combustion are CO_2 and water. However, by-products, including unburnt HC, CO, NOx, and particulate matters, are practically produced due to incomplete combustion. Although polluted emissions constitute only 1% of the total composition of diesel exhaust [5], the large number of diesel vehicles on the roads worldwide has turned it into a critical issue. Numerous solutions have been applied to reduce harmful substances focusing on pre-combustion, combustion, post-combustion. In pre-combustion stage, biodiesels made from palm, soybean, and sunflower are commonly used as practical solutions for advanced combustion due to their high oxygen

Appendix D

AUTHOR BIOGRAPHY

Author Mr. Dang Quang Huy

Nationality Vietnamese

Email 65016115@kmitl.ac.th

Education

2024 Master of Engineering in Automotive and Advanced Transportation Engineering, School of Engineering, King Mongkut's Institute of Technology Ladkrabang.

2020 Bachelor of Engineering in Mechanical Engineering, College of Engineering, Can Tho University.

Publication

Dang, Q. H., Karin, P., Cosh, P. T., et al. (2024). Impact of Partial-Flow Particulate Filter on Emissions from a Light-Duty Diesel Vehicle. In *Proceedings of the 13th TSME International Conference on Mechanical Engineering,* Thailand, 125-134.